
[All ETDs from UAB](#)

[UAB Theses & Dissertations](#)

2004

Analytical methods of laser spectroscopy for biomedical applications.

Dmitri V. Martyshkin
University of Alabama at Birmingham

Follow this and additional works at: <https://digitalcommons.library.uab.edu/etd-collection>

Recommended Citation

Martyshkin, Dmitri V., "Analytical methods of laser spectroscopy for biomedical applications." (2004). *All ETDs from UAB*. 5274.
<https://digitalcommons.library.uab.edu/etd-collection/5274>

This content has been accepted for inclusion by an authorized administrator of the UAB Digital Commons, and is provided as a free open access item. All inquiries regarding this item or the UAB Digital Commons should be directed to the [UAB Libraries Office of Scholarly Communication](#).

ANALYTICAL METHODS OF LASER SPECTROSCOPY FOR BIOMEDICAL
APPLICATIONS

by

DMITRI V. MARTYSHKIN

A DISSERTATION

Submitted to the graduate faculty of The University of Alabama at Birmingham,
in partial fulfillment of the requirements for the degree of
Doctor of Philosophy

BIRMINGHAM, ALABAMA

2004

UMI Number: 3149780

INFORMATION TO USERS

The quality of this reproduction is dependent upon the quality of the copy submitted. Broken or indistinct print, colored or poor quality illustrations and photographs, print bleed-through, substandard margins, and improper alignment can adversely affect reproduction.

In the unlikely event that the author did not send a complete manuscript and there are missing pages, these will be noted. Also, if unauthorized copyright material had to be removed, a note will indicate the deletion.

UMI[®]

UMI Microform 3149780

Copyright 2005 by ProQuest Information and Learning Company.

All rights reserved. This microform edition is protected against unauthorized copying under Title 17, United States Code.

ProQuest Information and Learning Company
300 North Zeeb Road
P.O. Box 1346
Ann Arbor, MI 48106-1346

ABSTRACT OF DISSERTATION
GRADUATE SCHOOL, UNIVERSITY OF ALABAMA AT BIRMINGHAM

Degree Ph.D Program Physics

Name of Candidate Dmitri V. Martyshkin

Committee Chair Sergey B. Mirov

Title Analytical Methods of Laser Spectroscopy for Biomedical Applications

Different aspects of the application of laser spectroscopy in biomedical research have been considered. A growing demand for molecular sensing techniques in biomedical and environmental research has led the introduction of existing spectroscopic techniques, as well as development of new methods. The applications of laser-induced fluorescence, Raman scattering, cavity ring-down spectroscopy, and laser-induced breakdown spectroscopy for the monitoring of superoxide dismutase (SOD) and hemoglobin levels, the study of the characteristics of light-curing dental restorative materials, and the environmental monitoring of levels of toxic metal ion is presented. The development of new solid-state tunable laser sources based on color center crystals for these applications is presented as well.

ACKNOWLEDGMENTS

I wish to express my gratitude to my advisor, Dr. Sergey Mirov, for his continuous guidance. I am thankful to my graduate committee members, Drs. Renato Camata, Joseph Harrison, Juan Pablo Claude, John Crow, and Joseph Beckman. Without their unyielding assistance this work would not be possible. I also thank the members of the laser lab: Dr. Vladimir Fedorov, Dr. Anatoliy Kudryavtsev, Igor Moskalev, and W. Blake Martin. I also thank Dr. David Shealy, Dr. Yogesh K. Vohra, Dr. Thomas Nordlund, and the Physics Department for the unique opportunity of studying at UAB and using these excellent facilities. I thank Dr. R. C. Ahuja for the opportunity to work with a state-of-the-art gated CCD camera, and J. G. Parker for his contribution.

TABLE OF CONTENTS

	<i>Page</i>
ABSTRACT.....	ii
ACKNOWLEDGMENTS	iii
LIST OF TABLES.....	vii
LIST OF FIGURES	viii
LIST OF ABBREVIATIONS.....	xii
INTRODUCTION	1
APPLICATION OF NOVEL DETECTORS IN TIME-RESOLVED SPECTROSCOPY	6
Suppression of fluorescence light in Raman measurements using ultrafast time-gated CCD camera.....	6
Introduction.....	6
Experimental	9
Instrumentation	9
Samples preparation.....	10
Results and analysis	10
Rejection of fluorescence.....	10
Rejection of stray-light and luminescence.....	15
Conclusions.....	20
LIGHT SOURCES.....	21
Tunable distributed feedback color center laser using stabilized F_2^{+**} color centers in LiF crystal.....	21
LiF: F_2^{+**} tunable color center laser based on littrow cavity	27
PRACTICAL APPLICATIONS OF LASER SPECTROSCOPY METHODS IN BIOMEDICAL RESEARCH AND ENVIRONMENTAL MONITORING	32
Laser spectroscopy study of superoxide dismutase (SOD).....	32

TABLE OF CONTENTS (Continued)

	<i>Page</i>
Fluorescence assay for monitoring Zn-deficient superoxide dismutase <i>in vitro</i>	32
Introduction.....	32
Material and Methods	36
Absorption.....	36
Fluorescence	37
Conclusions.....	42
Surface enhanced Raman (SERS) study of superoxide dismutase (SOD)	44
Introduction.....	44
Metal colloids as a SERS active substrate	46
Potential of SERS in biology and medicine.....	47
Detection of zinc-deficient superoxide dismutase with SERS and comparison with resonance Raman spectroscopy measurements.....	48
Experimental setup.....	50
Colloids preparation.....	51
Results.....	51
Conclusions.....	52
Study of SOD and hemoglobin by evanescent wave cavity ring-down spectroscopy.....	54
Introduction.....	54
Material and methods.....	54
Results.....	56
Hemoglobin.....	56
SOD.....	57
Raman study of degree conversion (DC) and depth of cure (PC) of dental restorative materials	59
Introduction.....	59
Materials and methods	60
Results.....	64
Conclusions.....	67
Laser breakdown spectrometer for environmental monitoring.....	67
Introduction.....	67
Experimental Arrangements	69
Water-argon gas aerosol LIBS measurements.....	74
Aluminum (Al).....	75
Cadmium (Cd)	75
Copper (Cu)	76
Iron (Fe)	77
Lead (Pb).....	77
Zinc (Zn).....	78

TABLE OF CONTENTS (Continued)

	<i>Page</i>
LIBS measurements when plasma is generated in the water jet of continuously circulating sample	79
Conclusions.....	81
CONCLUDING REMARKS.....	83
LIST OF REFERENCES.....	84
APPENDIX: CALCULATION OF THE DETECTION LIMIT OF MICRORAMAN IMAGING SYSTEM DILOR XY	90

LIST OF TABLES

<i>Table</i>	<i>Page</i>
1 The output power density at different wavelength and corresponding irradiation times	61

LIST OF FIGURES

<i>Figure</i>	<i>Page</i>
1 Raman system optical setup.....	10
2 Raman spectrum of HBC obtained with ungated CCD camera.....	11
3 Time-resolved HBC fluorescence and Raman scattering signal.....	12
4 Time-resolved fluorescence and Raman spectra of HBC powder.....	14
5 Stray-light and fluorescence rejection from HBC powder.....	14
6 Linear fit of natural logarithm of HBC fluorescence intensity.....	15
7 Raman spectra of CaWO ₄ crystal obtained with ungated CCD camera.....	16
8 Time-resolved total light intensity obtained with gated CCD camera.....	17
9 Time-resolved intensity of Raman bands of CaWO ₄ crystal.....	18
10 Time-resolved Raman spectra of CaWO ₄ crystal.....	19
11 Stray light and fluorescence rejection from CaWO ₄ crystal by a time-resolved light detection.....	19
12 Absorption spectrum of LiF:F ₂ ⁺⁺⁺ color center crystal.....	23
13 Experimental setup of LiF:F ₂ ⁺⁺⁺ DFB laser.....	24
14 Tunable operation of LiF:F ₂ ⁺⁺⁺ distributed feedback laser.....	25
15 The output energy of LiF:F ₂ ⁺⁺⁺ DFB laser with respect to pumping pulse energy.....	25
16 Temporal delay of LiF:F ₂ ⁺⁺⁺ DFB laser emission with respect to pumping pulse.....	26
17 LiF:F ₂ ⁺⁺⁺ DFB laser linewidth measurements.....	26

LIST OF FIGURES (Continued)

<i>Figure</i>	<i>Page</i>
18 Littrow cavity.....	28
19 The autocollimation angles (A) and of the angular dispersion (B) dependences	29
20 Double pump pass Littrow scheme of the LiF:F ₂ ^{***} laser with intracavity telescope.....	31
21 Interference fringe pattern of spectral output of LiF laser based on 29 cm Littrow resonator with intracavity 3x telescope measured with F-P etalon.....	31
22 Absorption spectra of (a) mixture of D124N SOD1 0.8 mg/mL, BCDS 0.1 mM, and ascorbic acid 0.05 mM, (b) mixture of 0.05 mM CuSO ₄ , 0.1 mM BCDS, and 0.05 mM ascorbic acid (c) mixture of metal replete wild-type SOD1 (0.8 mg/ml), 0.1 mM BCDS, and 0.05 mM ascorbic acid, in 100 mM potassium phosphate buffer.....	37
23 Fluorescence spectrum of BCDS in 100 mM potassium phosphate buffer excited at 482 nm	38
24 Fluorescence spectrum of the BCDS complex with free Cu ¹⁺ in 100 mM potassium phosphate buffer excited at 482 nm.....	39
25 Fluorescence spectrum of the BCDS complexes with D124N (zinc-deficient) SOD1 excited at 482 nm.....	39
26 Deconvoluted spectrum of BCDS fluorescence	40
27 Deconvoluted spectrum of (BCDS) ₂ -Cu ¹⁺ complexes fluorescence	40
28 Deconvoluted spectrum of the BCDS/Cu ¹⁺ -SOD1 (D124N mutant) complexes fluorescence	41
29 Intensity of the 734 nm fluorescence band of the BCDS/Cu ¹⁺ -SOD1 (D124N mutant) complexes as a function of concentration	42
30 Experimental Setup for SOD Raman studies.....	50
31 SERS spectra of a) zinc-deficient SOD1 and b) Cu,Zn SOD1	53
32 LiF:F ₂ ^{***} tunable color center laser.....	55
33 Experimental setup for the EW-CRDS measurements	55

LIST OF FIGURES (Continued)

<i>Figure</i>	<i>Page</i>
34 Ring-time dependence on concentrations of hemoglobin at different adsorption times	56
35 Same as in Fig. 34 with zoomed low concentration region for the convenience.....	57
36 Dependence of ring-down time from concentration of BCDA-Cu ¹⁺ complexes after 15 minutes of adsorption	58
37 Kinetics of BCDA-Cu ¹⁺ complexes adsorption on the prism surface	58
38 Experimental setup used for composites curing by a different wavelength	61
39 Reconstruction of Raman spectrum of uncured Esthet X composite with a Gaussian deconvolution method	63
40 Reconstructed Raman spectra uncured Esthet X composite and Esthet X composite cured by QTH lamp.....	64
41 Degree of conversion (DC) of Esthet X, Shade A2 composite for the different wavelength of curing light	65
42 Degree of conversion (DC) of TPH, Shade A2 composite for the different wavelength of curing light	65
43 The absorption (attenuation) spectra of a) TPH, shade A2 composite material and b) Esthet X, shade A2 composite material.	66
44 Emission spectrum of Spectrum 800 (Dentsply) curing light.....	66
45 LIBS System Design with argon-water aerosol sample delivery	71
46 LIBS System Design with direct generating plasma in the water jet of a continuously circulating sample	72
47 Time evolution of the LIBS spectrum for water containing 500 ppb Cu	73
48 Spatially resolved LIBS spectrum of Cu (10-ppm) contaminated water sample generated by the Nd:YAG laser and measured at distances 5, 3, 2, 1, 0, and -1 mm from the continuous flowing water jet.....	74
49 LIBS signal corresponding to Al line 394.4006 nm vs. "LIBS-determined" concentration (mg/L)	75

LIST OF FIGURES (Continued)

<i>Figure</i>	<i>Page</i>
50 LIBS signal corresponding to Cd line at 228.8022 nm vs. "LIBS-determined" concentration (mg/L).....	76
51 LIBS signal corresponding to Cu line at 324.754 nm vs. "LIBS-determined" concentration (mg/L).....	76
52 LIBS signal corresponding to Fe line at 248.327 nm vs. "LIBS-determined" concentration (mg/L)	77
53 LIBS signal corresponding to Pb line at 405.78 nm vs. "LIBS-determined" concentration (mg/L)	78
54 LIBS signal corresponding to Zn line at 213.856 nm vs. "LIBS-determined" concentration (mg/L)	78
55 LIBS signal for Cu polluted water vs. "LIBS-determined" concentration (ppb).....	80

LIST OF ABBREVIATIONS

AAS	atomic absorption spectrophotometer
ALS	amyotrophic lateral sclerosis
BCDS	bathocuproine disulfonate
CC	color center
CCC	color center crystals
CCD	charge-coupled device
CRDS	cavity ringdown spectroscopy
DC	degree of conversion
DFB	distributed feedback
EW-CRDS	evanescent wave cavity ringdown spectroscopy
FWHM	full width half maximum
HBC	hexobenzocoronene
IR	infrared radiation
LIF	laser-induced fluorescence
LIBS	laser-induced breakdown spectroscopy
NO	nitric oxide
PC	depth of cure
QTH	quartz-tungsten-halogen
SERS	surface enhanced Raman spectroscopy
SOD	superoxide dismutase

INTRODUCTION

The majority of knowledge about the structure of atoms and molecules is based on spectroscopic studies. Spectroscopy has made an outstanding contribution to the present state of molecular and atomic physics, chemistry, and molecular biology.

Information on molecular structure and interaction may be obtained in many ways from the absorption or emission spectra generated due to the interaction of electromagnetic radiation with matter. The measurements of wavelength of the spectral line provide information regarding the energy levels of the atomic or molecular system. The intensity of spectral lines is proportional to the transition probability and, hence, is useful for verification of a spatial charge distribution of the excited electrons, which can be only roughly estimated for the multiatom molecules. Measurements of spectral linewidth yield information on molecular velocity distribution, temperature, collision processes, and interatomic potentials. Zeeman and Stark splitting are important for the measurements of magnetic and electric moments and for elucidating the coupling of different angular momenta in atoms and molecules. The hyperfine structure yields information regarding the interaction between nuclei and the electron cloud. Time-resolved measurements reveal lifetimes of excited state, allow studying of dynamical processes, and allow the investigation of the collision processes and various energy transfer mechanisms. These examples are only a small number of the many possible ways in which spectroscopy can be applied to get insight into a micro-world of atoms and molecules. The application of new technologies to optical instrumentation has significantly extended the sensitivity limits of

classical spectroscopy methods. However, the most stimulating impetus was given to the entire field of spectroscopy with the introduction of lasers. The spectral resolution and sensitivity of classical spectroscopy methods were boosted several orders of magnitude, and many new spectroscopic techniques appeared that were impossible to perform without a coherent light source.

Several examples will be given to illustrate the advantage of laser utilization. In classical absorption spectroscopy (Doppler limited), radiation sources with a broad emission are used, such as high-pressure Hg and Xe lamps. Transmitted light is measured with a detector after passing through a dispersing element (spectrometer or interferometer), so that the value $\Delta I/I$, where I is incident light intensity, can be obtained. For the relatively weak absorption, the absorption coefficient α can be approximated as $\alpha = (\Delta I/I) \times (1/L) \times (\Delta\omega/\delta\omega)$, where $\delta\omega$ is a linewidth of the absorption, $\Delta\omega/\omega$ is a spectral resolution of dispersing element, and L is a length of spectroscopic cell. The conventional 1-m spectrograph with a resolution about 0.01 nm and a gas sample with $\delta\omega = 6$ GHz will give $\Delta\omega/\delta\omega = 10$. If one uses a 10-cm spectroscopic cell, the value of 10^{-6} cm^{-1} can be achieved for the lowest detectable absorption coefficient. However, if a single-mode tunable laser is used instead of lamp and spectrograph, one may reach $\Delta\omega < \delta\omega$, and the absorption coefficient detection limit is down to 10^{-9} cm^{-1} . That is a three orders of magnitude improvement due to the use of a laser as a light source. The sensitivity and resolution of absorption spectroscopy could be substantially improved with the use of lasers.

Cavity ring-down spectroscopy (CRDS) was developed more than 30 years ago. It was initially used for measurements of dielectric mirrors reflection. However, during the

last 10 years, it was developed to a new, very sensitive detection technique for the measuring of small absorption. The method is based on measuring the decay times of laser pulses in a optical resonator filled with absorbing molecules. The detection limit of the absorption achieved was as small as 10^{-10} cm^{-1} , and resolution reached $\delta\nu \sim 10^7 \text{ s}^{-1}$, which is less than the Doppler width of absorption lines.

Excitation of single atomic levels was achieved in fluorescence spectroscopy with hollow cathode lamps even before the invention of laser. However, in molecular spectroscopy, only accidental coincidences between the atomic resonance lines of the hollow cathode lamp and the molecular transitions of the sample could be used. On the contrary, narrow band lasers could be tuned to every wanted molecular transition.

The introduction of lasers gave rise to new types of spectroscopy, such as laser spectroscopy in molecular beams, optical pumping and double resonance techniques, time-resolved laser spectroscopy, and coherent spectroscopy.

There is a huge demand for modern molecular sensing methods. They are used in many research and commercial applications, such as biology, chemistry, physics, medical care, environmental monitoring, the military, and homeland security. The development of a sensitive and reliable method is an interdisciplinary task and requires a contribution from practically all branches of natural science.

The progress in laser technology leads to subsequent progress in laser biomedical applications and biotechnology. The special properties of laser light are spatial and temporal coherence (directivity and focusability), high intensity in both cw and pulsed modes of operation, monochromaticity, tunability, and short pulse duration. One can vary laser radiation parameters (wavelength, intensity, and duration) over very wide limits, making it possible to implement various light-biomatter interactions (linear and nonlinear, single

and multi-photon, and coherent and noncoherent), thus inducing various effects in biological tissues (e.g., photochemical modifications, thermal distraction, ablation, optical breakdown, and shock waves.).

All laser biomedical diagnostics can be subdivided into two classes: (a) macro-diagnostics of various objects and (b) micro-diagnostics (spectral) at different organization levels from organs and cells to biomolecules.

Spectral diagnostics on the molecular level use a wide variety of laser spectroscopy methods that enable one to obtain parameters inaccessible without the use of laser radiation.

1. Spectral resolution may reach any desired value from nanometers to MHz. A high spectral resolution combined with a high sensitivity may be used in, for example, CRDS, to detect gas phase products of metabolism for diagnostics of certain diseases.

2. Temporal resolution has reached fs with development of ultrashort laser pulses. Ultrafast laser spectroscopy greatly contributes to our understanding of fundamental processes in biological systems, such as electron and energy transport in photosynthesis and reaction centers, and proton transfer in pigments and cell membranes. The combination of time-resolved spectroscopic techniques with a laser-scanning microscope creates a chance to study a dynamical process with a high spatial resolution.

3. Sensitivity of detection of atoms and molecules can reach the ultimate limit, i.e. the single-molecule level. Highly sensitive fluorescence methods are used to diagnose diseases at a cellular level.

4. Selectivity of laser spectroscopy methods can be very high and enables one to detect traces of certain molecules in the environment, organisms, and the human body.

5. The spatial resolution at wavelength level is standard in confocal microscopy

methods that are widely used in biomedicine. Laser-induced fluorescence spectroscopy, Raman spectroscopy, and their combination have proven to be very helpful in a determination of the structure of biological molecules. Many of the spectroscopy techniques can be applied in combination with a microscope, giving an additional advantage of spatial resolution. New methods, such as near-field laser microscopy and photoelectron spectral microscopy, are being searched in order to find a way to increase spatial resolution up to the nanometer range.

This manuscript summarizes the work that was done towards the understanding of the most recent spectroscopic techniques, their practical applications in biomedical research, and the development of new methods. The chapters are grouped in the following manner: Application of novel detectors in time-resolved spectroscopy, Light sources, and Practical applications of Laser Spectroscopy methods in biomedical research and environmental monitoring. The last chapter is the most significant part of the manuscript. It contains the results of laser spectroscopy study (fluorescence, Raman, and CRDS) of superoxide dismutase (SOD), Raman study of degree conversion (DC) and depth of cure (PC) of dental restorative materials, and a study toward the development of a novel laser breakdown spectrometer for environmental monitoring.

The material in the sections regarding tunable distributed feedback color center laser using stabilized F_2^{+**} color centers in LiF crystal, the suppression of fluorescence light in Raman measurements using ultrafast time-gated CCD camera, a fluorescence assay for monitoring Zn-deficient superoxide dismutase *in vitro*, and the laser breakdown spectrometer for environmental monitoring, was published previously and therefore, is presented in a modified form in this manuscript. The original publications can be found in Refs. 1 to 4.

APPLICATION OF NOVEL DETECTORS IN TIME-RESOLVED SPECTROSCOPY

Suppression of fluorescence light in Raman measurements using ultrafast time-gated CCD camera

Introduction

Raman spectroscopy is one of the most powerful methods for the characterization of molecules. Raman spectroscopy could be the first choice for many scientists and engineers due to its high information content in comparison with many other methods. For many years it has been used as an analytical tool and a method for studying the physical and chemical properties of various materials. Due to recent developments in laser and detector technologies, some of the limitations of this method have been overcome, attracting a lot of attention in research and industrial laboratories worldwide.

Raman spectroscopy has certain drawbacks and limitations, like any other spectroscopic technique. The major disadvantage is a low ($\sim 10^{-30}$ cm²) cross-section of Raman scattering. The Raman signal is weak compared to the fluorescence background and is hard to detect. There are several common methods dealing with the discrimination of Raman scattering from fluorescence, thermal radiation, and stray light.

The out-of-focus background due to fluorescence of fluorophores distributed over sample volume and stray light could be effectively suppressed, as in confocal Raman microscopy [5]. However, highly fluorescent samples are still beyond the scope of this method.

Another method of fluorescence background suppression is the use of UV light for sample excitation [6,7]. The Stokes shifts of the Raman scattering are usually smaller than the fluorescence Stokes shift, if excited by UV radiation, permitting effective spec-

tral discrimination of fluorescence. In addition, the majority of molecules have electronic transitions in the UV region, providing the conditions for resonance Raman scattering and enhancing intensity of Raman bands up to several orders of magnitude [6,7]. However, the problems associated with samples degradation and the resonance excitation of fluorescence makes this method appropriate for a relatively small class of molecules.

Fluorescence excitation could be avoided by tuning the laser wavelength far away from electronic transitions to near infrared region, as is done in Fourier-transformed Raman spectroscopy. On the other hand, the Raman signal decreases as wavelength in negative fourth power, and some organic samples have a strong fluorescence even in the near IR region. In addition, Fourier-transformed Raman spectroscopy provides a relatively poor signal to noise ratio.

Not every laboratory is equipped with a confocal microscope. The use of a simple spectroscopic system immediately brings in the problem of the rejection of stray light. Usually, the stray light is associated with the elastic scattering of laser radiation, the autofluorescence of cements and coatings in optical elements, multiple reflections in optical elements and the spectrometer, and Rayleigh scattering in samples. This problem is especially crucial for the systems equipped with low-resolution spectrometers.

The standard approach to rejecting excitation radiation is the use of a notch filter. It effectively suppresses a part of radiation that propagates collinear to the optical axis. Otherwise, scattered light can propagate through a notch filter, substantially increasing background. However, those photons have longer optical path than Raman photons and therefore are delayed.

The alternative approach is time-resolved detection. It is based on the use of pulsed excitation and gated signal detection for the Raman scattering discrimination from

fluorescence [8], thermal radiation [9], and stray light in time domain. Fluorescence lifetimes are in nanoseconds or a longer temporal range for the majority of molecules, while the Raman scattering occurs almost instantaneously with a laser pulse. The picosecond excitation pulse and subnanosecond signal gating provide an effective elimination of the fluorescence signal, broad in time domain. The number of Raman photons collected in a picosecond gate width would be extremely small. Therefore, the detection system should have a high-duty cycle in order to obtain a reasonable signal-to-noise ratio.

Time-resolved detection of Raman scattering has been attracting a considerable attention for a few decades. Nevertheless, due to technological limitations it was impracticable until recently. A brief review can be found in Ref. 6. Two different approaches of time-resolved detection have been shown to be effective for obtaining Raman spectra from fluorescent samples.

In the first method Matousek *et. al* used a Kerr gate with a ~ 3 -ps resolution at a 650-Hz repetition rate and a spectrometer-CCD detector combination for the light detection [10,11]. The suppression of a fluorescence background with a lifetime about 2 ns by three orders of magnitude was achieved. The average power of laser radiation may only be a few mW, due to a high peak power (MW), which can induce sample damage and nonlinear processes. In the second approach, Tahara *et al.* used a streak-camera and achieved resolution of about 10 ps at up to a 2-kHz repetition rate for a fluorophore with a fluorescence lifetime 4 ns [12].

The duty cycle of the detection system could be improved by several orders of magnitude due to recent advances in laser and detector technologies. Our approach of time-resolved detection of Raman scattering is based on a combination of the state-of-the-art intensified/gated CCD camera (LaVision "PicoStar HR"), the ultrafast Ti:sapphire

oscillator, and a simple spectrograph with a short focal length. The system has a 150-ps temporal resolution at a 76-MHz repetition rate with the average power of laser radiation up to 300 mW without noticeable sample damage. An effective rejection of fluorescence and stray light background was demonstrated for clear crystalline samples, as well as for heterogeneous (powder-like) samples.

Experimental

Instrumentation. Figure 1 shows the optical setup of the Raman system. The excitation radiation was focused to a spot of approximately 400 μm through a 45-degree mirror. The scattered radiation was collected using 180 degrees scheme. The super-notch filter (785 nm, Kaiser Corp.), placed inside a two-lens collimator, was used to suppress elastically scattered excitation radiation. The radiation of the Ti-sapphire laser (Coherent, Mira Model 900-P Laser) at 785 nm with a 2-ps pulse duration at a 76-MHz repetition rate was used for excitation. The average power used for sample excitation was about 300 mW.

The Acton Research "SpectroPro-150" single grating spectrograph with a focal length of 150 mm, 1200 g/mm grating, f/4 aperture ratio, and 16 cm^{-1} resolution, combined with one of two CCD cameras described below, was used for the Raman scattering detection.

The PicoStar HR (LaVision) is intensified gated/modulated CCD camera system with image intensifier designed for fast gating at a repetition rate up to 110 MHz. The gate width is less than 200 ps and the jitter less than 20 ps. The photocathode sensitivity is in the 400-900 nm range. The system is equipped with a CCD chip (Interline, 1376 \times

1040 pixels) with ultrafast readout rate capability (16 MHz pixel, or 10 frames/s) and 65% maximum quantum efficiency. The second CCD was a thermoelectric cooled camera (Princeton Instruments) with a mechanical shutter.

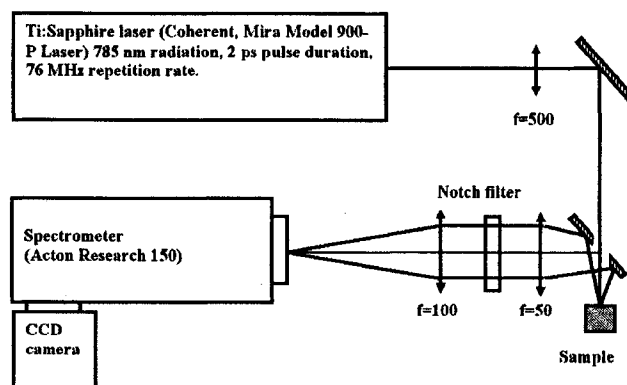


FIG. 1. Raman system optical setup.

Samples preparation. Two highly fluorescent samples have been used in this study. The crystalline CaWO_4 with Nd^{3+} impurities and hexobenzocoronane (HBC) powder were used as transparent and heterogeneous sample, respectively. Both samples exhibited a strong fluorescence under 785 nm excitation.

Results and Analysis

Rejection of fluorescence. The heterogeneous samples usually exhibit a strong elastic scattering of excitation radiation. The scattered light experiences diffuse reflection, considerably increasing out-of-focus fluorescence background and a signal due to a stray light. The hexobenzocoronane (HBC) spectrum of obtained with the ungated CCD

camera is shown in Fig. 2. The spectrum was an average of 50 acquisitions of one s each. HBC has a strong fluorescence, even under near IR excitation. The background signal tremendously veiled a weak Raman scattering signal at 1304 cm^{-1} .

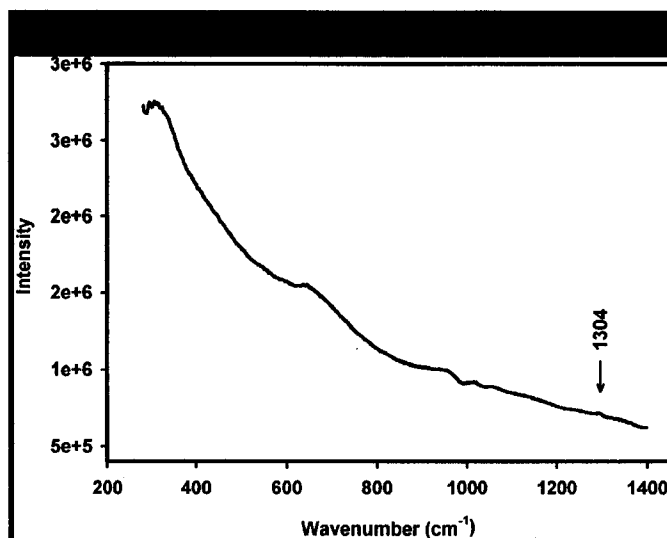


FIG. 2. Raman spectrum of HBC obtained with ungated CCD camera. The weak band at 1304 cm^{-1} corresponds to HBC Raman scattering. The other bands and strong background are due to a stray light and fluorescence.

The time-resolved signal at around 1178 cm^{-1} and 1304 cm^{-1} obtained with a gated CCD camera is demonstrated in Fig. 3 (I, II). The spectrum was obtained with a 150-ps gate width and a 25-ps temporal step between data points. Figure 3 shows that a signal around 1304 cm^{-1} is presumably a combination of HBC Raman bands and fluorescence, while a signal at 1178 cm^{-1} corresponds only to fluorescence. Two bands have a similar behavior at a gate delay longer than 300 ps, as can be seen in Fig. 3(I). Since Raman scattering could not be detected at such a long gate delay, one can see fluorescence decay only. In contrast, at a shorter delay, as shown in Fig. 3(II), a signal around 1304 cm^{-1} rises faster than a fluorescence signal around 1178 cm^{-1} , demonstrating the existence

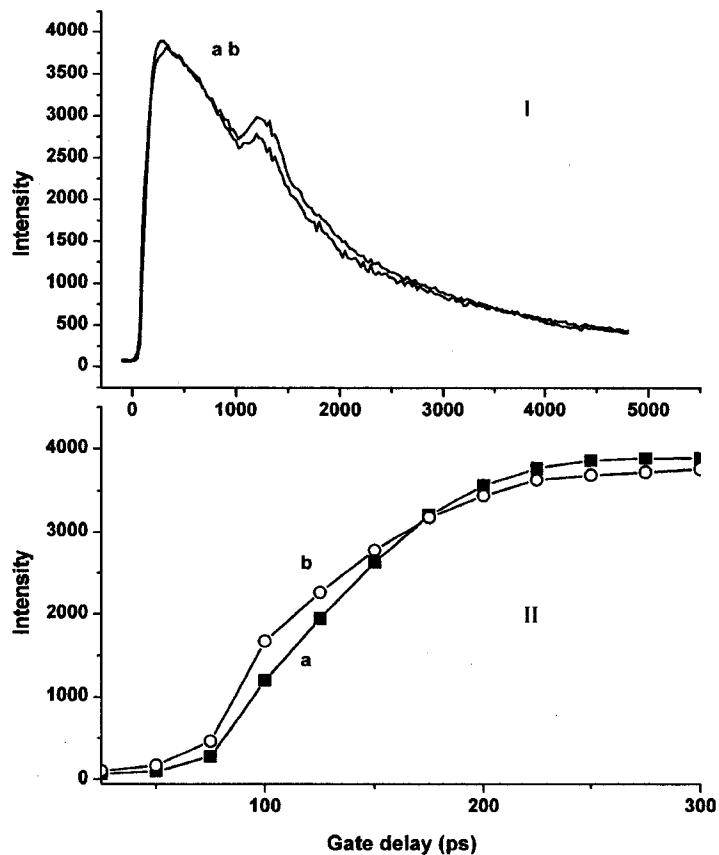


FIG. 3. Time-resolved HBC fluorescence and Raman scattering signal at a) 1178 cm^{-1} and b) 1304 cm^{-1} . The full-scale signal is shown in (I), while the zoomed initial part of the same kinetics is shown in (II). The signal at a) 1178 cm^{-1} corresponds to HBC fluorescence only, while the signal at b) 1304 cm^{-1} is a superposition of fluorescence and Raman scattering. The signal at 1304 cm^{-1} rises faster than the signal at 1178 cm^{-1} , due to additional Raman scattered light. The band at 1200 ps is an artifact, due to stray light.

of the additional component corresponding to a Raman scattered light at 1304 cm^{-1} . The spike at 1200 ps is an artifact due to a stray light.

Figure 4 shows time-resolved Raman and fluorescence spectra of HBC. Each spectrum has an average of 50 acquisitions, and spectra were obtained with a 150-ps gate width at different gate delays. Raman bands start to emerge at a 50-ps delay together with a broad fluorescence signal. Raman bands were the most distinct at 100 and 150-ps gate delays and diminished completely at a 300-ps delay, so that only fluorescence can be seen. Figure 5 illustrates HBC Raman spectrum taken at a 100-ps gate delay after fluorescence background subtraction. The achieved signal-to-background ratio was greater than 100 for a strongly fluorescent powder sample with a relatively short fluorescence lifetime. The simultaneous study of the emission of the fluorophores with a fluorescence lifetime in the nanosecond range in spectral and temporal domains is another important capability of an ultrafast time-gated detection method. This feature of the method is extremely important in biomedical applications, since the majority of endogenous fluorophores have a lifetime of about 1-5 ns.

The fluorescence kinetics depicted previously in Fig. 3 could be used for HBC fluorescence lifetime determination. We have used the data after a 2500-ps gate delay, since data before 2500 ps were contaminated with a stray light (details in the next section). The natural logarithm of fluorescence intensity and corresponding linear fit are shown in Fig. 6. The time constant was found to be $-4.8 \cdot 10^8\text{ s}^{-1}$, corresponding to 2.1 ns fluorescence lifetime.

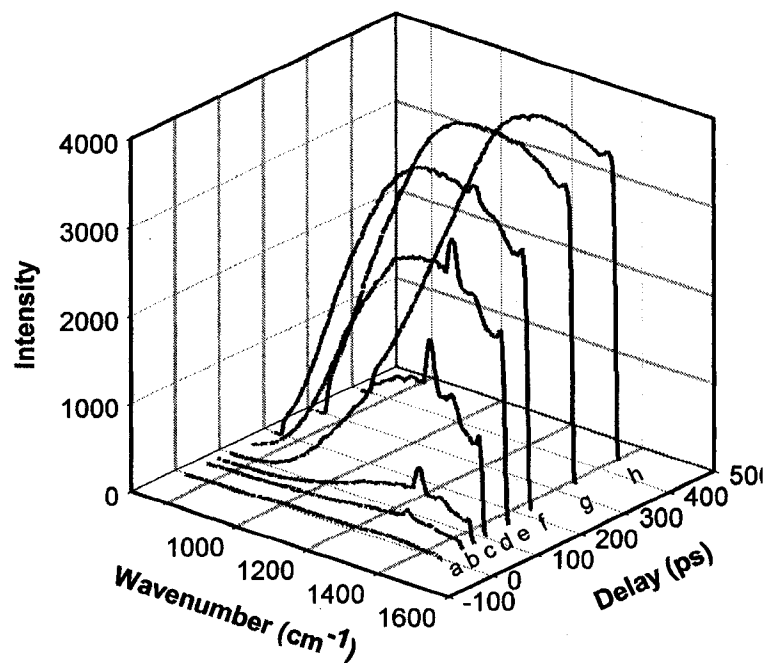


FIG. 4. Time-resolved fluorescence and Raman spectra of HBC powder. The spectra were taken at a) 0-, b) 50-, c) 75-, d) 100-, e) 150-, f) 200-, g) 300-, and h) 400-ps gate delays. Each spectrum is an average of 50 acquisitions.

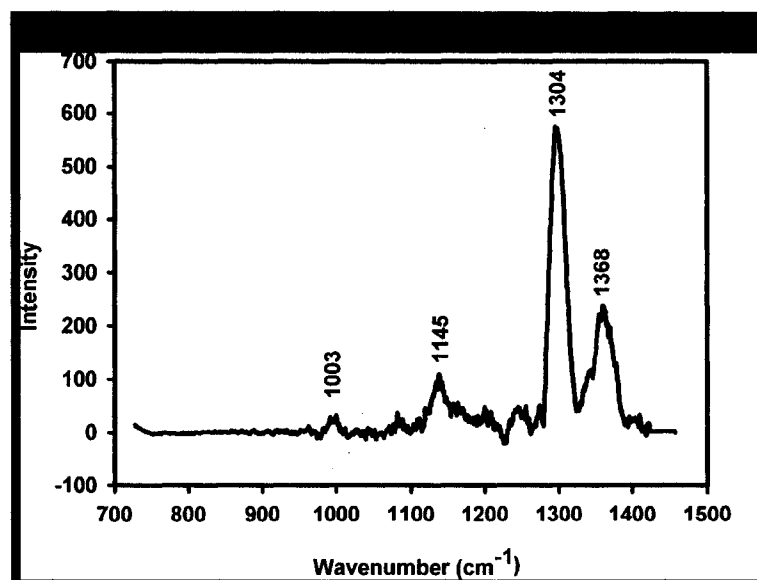


FIG. 5. Stray-light and fluorescence rejection from HBC powder. HBC Raman spectrum is obtained at a 100-ps gate delay. The spectrum is an average of 50 acquisitions. The fluorescence background is subtracted.

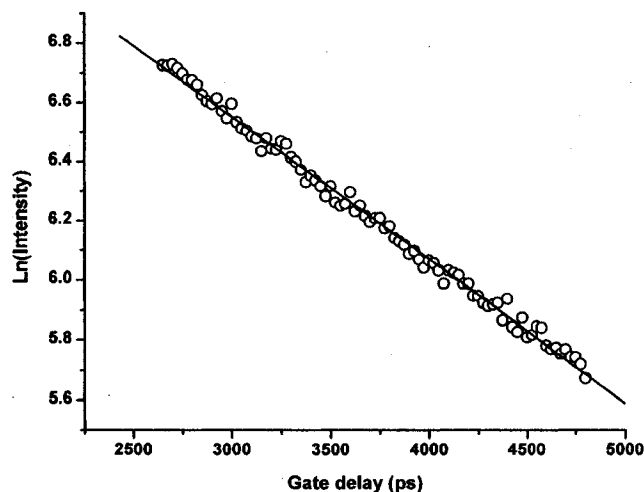


FIG.6. Linear fit of natural logarithm of HBC fluorescence intensity. The time constant was found to be $-4.8 \cdot 10^8 \text{ s}^{-1}$, corresponding to 2.1 ns fluorescence lifetime.

Rejection of stray-light and luminescence. The spectrum of CaWO_4 crystal contaminated with Nd^{3+} ions obtained with a conventional CCD camera is shown in Fig. 7. The stray-light and luminescence background substantially masked a weak Raman signal. The strongest 912-cm^{-1} Raman band of CaWO_4 corresponding to totally symmetric stretch vibrations of tetrahedrons WO_4^{2-} [13] has been resolved only. The strong band at 1270 cm^{-1} (873 nm) was due to the luminescence of Nd^{3+} (${}^4F_{3/2} \rightarrow {}^4I_{9/2}$) [14] ions. The stray-light inhomogeneously distributed over the CCD surface was the cause of the other bands presented in Fig. 7. A strong luminescence background and artifact bands due to a stray light strongly distort the Raman spectrum and make it impossible to resolve. We were able to significantly improve the signal-to-background ratio by rejecting stray-light and luminescence using a time-resolved signal detection.

The total intensity of light that reaches a detector at different times is shown in Fig. 8. The light was detected by a gated CCD camera in 100-ps temporal intervals and a

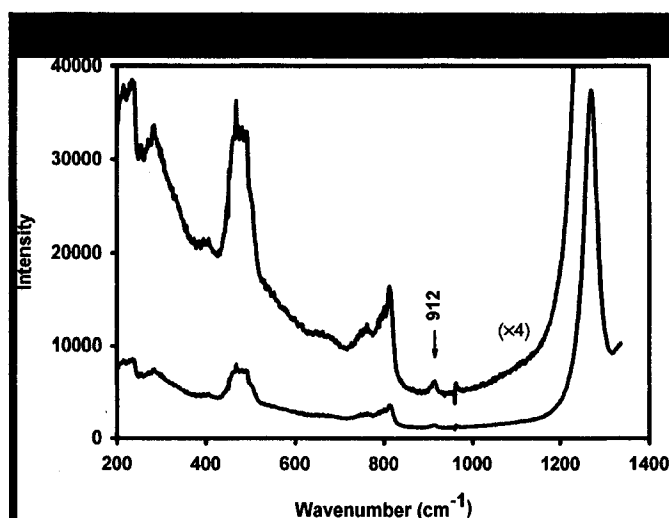


FIG. 7. Raman spectra of CaWO_4 crystal obtained with ungated CCD camera. The spectrum (a) is an average of 50 acquisitions of one second each. Spectrum (b) is the same as (a) multiplied by four. The 912 cm^{-1} band corresponds to the strongest Raman band of CaWO_4 crystal. The strong 1270 cm^{-1} band corresponds to the fluorescence of Nd^{3+} (${}^4F_{3/2} \rightarrow {}^4I_{9/2}$) ions, which present as an impurity introduced during the crystal growth process. The other bands are due to stray light inhomogeneously distributed over the CCD camera surface.

gate width of about 200 ps. The spectrometer grating was positioned in such a way that Rayleigh scattered excitation radiation could be detected. The picks at 200 ps and 13 000 ps correspond to a combination of Raman and elastically scattered light signals. Strong signals at 1200 ps and 14 000 ps correspond to a superposition of elastic scattered light in the sample and optical elements of the system, which propagate noncollinearly to the optical axis. It also includes stray-light, due to multiple reflections at the optical elements of the system. One can see that stray light is delayed from the Raman signal and could be effectively gated off. Therefore, time-resolved signal detection allows us an effective separation of Raman bands from stray light and from the luminescence background. The CaWO_4 crystal that we used has Nd ions introduced as an impurity during the crystal

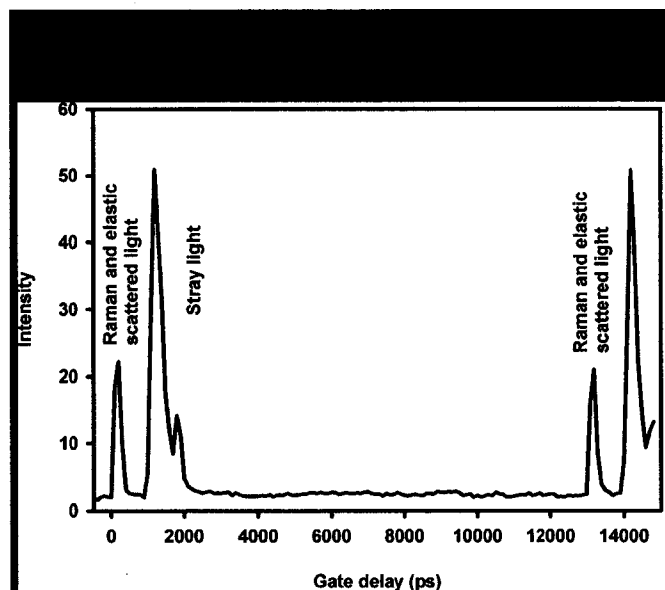


FIG.8. Time-resolved total light intensity obtained with gated CCD camera. The temporal step between consequent data points was 100 ps. The gate width was 200 ps. Signals at 200 ps and 1300 ps coincide with a laser pulse and correspond to Raman scattered light and elastic scattered light propagating collinear to optical axis, while strong signals at 1200 ps and 1800 ps correspond to overall stray light that reached the CCD camera.

growth process. The luminescence of rare-earth metal ions is usually narrow and could be easily confused with a Raman band if one uses a low-resolution spectrometer.

The time-resolved signals at around 797 cm^{-1} , 912 cm^{-1} , and 1280 cm^{-1} (873 nm) is demonstrated in Fig. 9. The spectrum was taken with a 200-ps gate width and a 25-ps temporal step between data points. The 797 cm^{-1} and 912 cm^{-1} correspond to the Raman band of CaWO_4 crystal. The signal profile has a symmetrical shape, with a temporal full width half maximum (FWHM) of about 200 ps, matching CCD camera gate width. In contrast, the signal at 1280 cm^{-1} (873 nm) was almost constant, corresponding to a luminescence of Nd^{3+} (${}^4F_{3/2} \rightarrow {}^4I_{9/2}$) ions, the lifetime of which is considerably longer ($\sim 250\text{ }\mu\text{s}$) than the interval between laser pulses (1 ns) and, therefore, intensity changes could not be seen in this temporal interval. A time-resolved Raman spectrum of CaWO_4 crystal

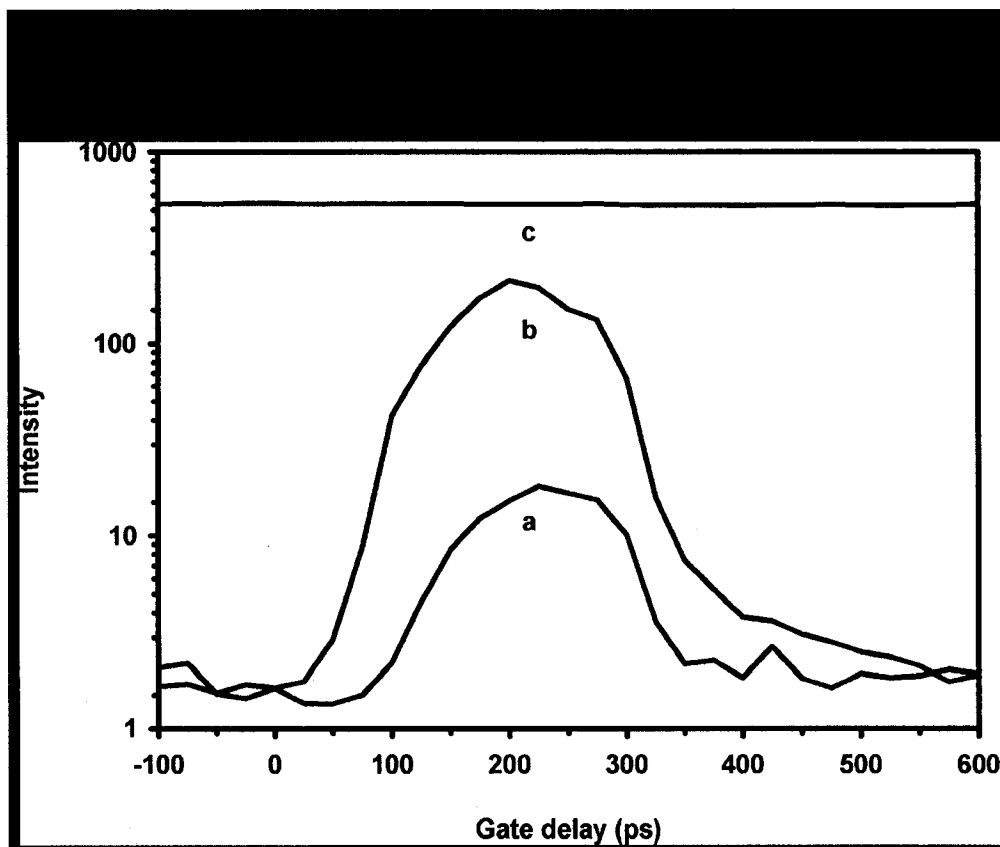


FIG. 9. Time-resolved intensity of Raman bands of CaWO_4 crystal at a) 797 cm^{-1} , b) 912 cm^{-1} , and c) luminance band at 873 nm (1280 cm^{-1}) of Nd impurities in CaWO_4 crystal. The temporal step between consequent data points was 25 ps. The gate width was 200 ps. The temporal FWHM of the Raman band is equal to 200 ps, corresponding to CCD gate width. The fluorescence intensity changes of Nd are not seen, since the fluorescence lifetime is substantially longer than the period of pump laser oscillations (1 ns).

obtained with a gated CCD camera is depicted in Fig. 10. The spectrograph grating was positioned in such a way that Nd impurities luminescence was out of the detection range. The strongest Raman signal was acquired at a 200-ps delay. Several CaWO_4 Raman bands, at 335 cm^{-1} , 405 cm^{-1} , 797 cm^{-1} , and 912 cm^{-1} , can be clearly resolved with an excellent signal-to-background ratio. Figure 11 shows a reconstructed CaWO_4 Raman spectrum obtained at a 200-ps gate delay and at different spectrometer grating positions. An excellent rejection of stray light and luminescence has been achieved.

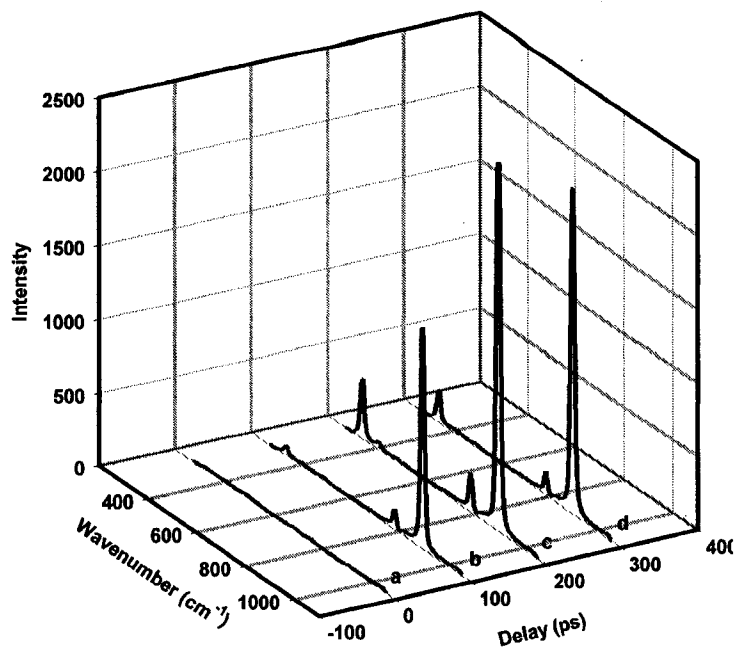


FIG. 10. Time-resolved Raman spectra of CaWO_4 crystal. The spectra were taken at a) 0-, b) 100-, c) 200-, and d) 300-ps gate delays.

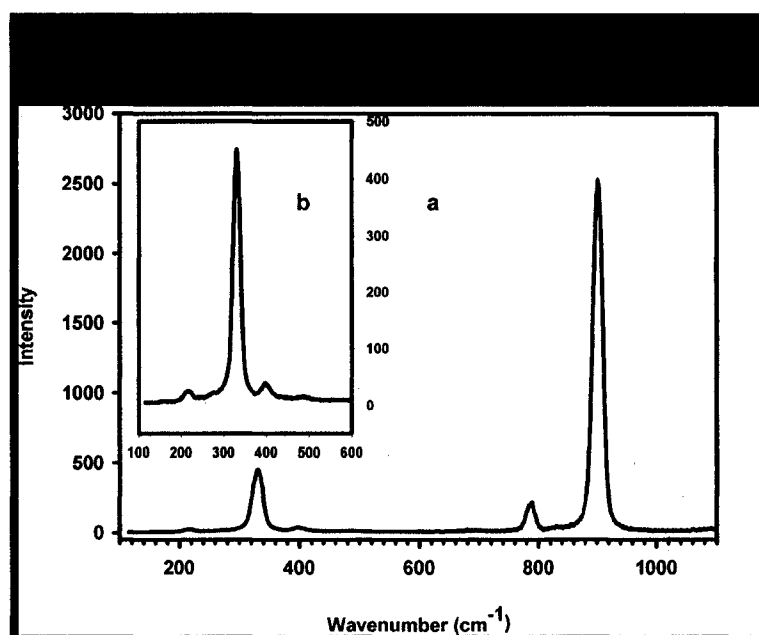


FIG. 11. Stray light and fluorescence rejection from CaWO_4 crystal by a time-resolved light detection. The spectrum (a) was combined from several spectra at different spectrograph grating positions. Two bands at 1280 cm^{-1} and 1400 cm^{-1} correspond to $\text{Nd}^{3+} ({}^4F_{3/2} \rightarrow {}^4I_{9/2})$ luminescence at 873 nm and 882 nm , respectively. Spectrum (b) is expanded spectrum (a) in $100\text{-}600\text{ cm}^{-1}$ spectral region.

Conclusions

Established time-resolved technique considerably improves signal-to-background ratio and extends the capabilities of Raman measurement toward the study of samples with short fluorescence lifetimes. We have shown that background from powder material related to stray light and fluorescence can be significantly suppressed even for a simple spectroscopic system equipped with a low-resolution spectrograph and gated CCD camera. The Ti-sapphire laser radiation at 785 nm and average power up to 300 mW was used for excitation without noticeable sample damage. The high-duty cycle (repetition rate 76 MHz) makes this technique superior comparing to other time-resolved Raman techniques. The advances in laser and detector technologies have created an opportunity to build a simple spectroscopic system able to solve multitasking problems. Simultaneous study of light emission from the variety of materials in spectral as well as in temporal domains opens an exciting opportunity to build a versatile instrument. The confocal microscope combined with a gated CCD camera will allow for the performance of Raman, resonance Raman, conventional, and time-resolved fluorescence imaging. That kind instrument may have extensive applications in many academic and industrial laboratories.

LIGHT SOURCES

Tunable distributed feedback color center laser using stabilized F_2^{+**} color centers in LiF crystal

Since being introduced for the first time by Kogelnik and Shank in the 1970s [15,16], distributed feedback (DFB) lasers have attracted substantial attention due to their simplicity, good mode selection, and easy tuning. Tunable operation of the DFB lasers in the visible spectral range was successfully demonstrated using different organic dyes [17-22] as active media. Recently, tunable DFB laser operation in the UV range was achieved by using Ce^{3+} doped materials [23]. Color center crystals (CCC) are the most promising active media for the DFB tunable solid state lasers in the infrared (IR) range. CCC have high emission cross-sections, in the same order of magnitude with cross-sections of organic dyes, and broad tunability in the near-infrared and the IR spectral regions.

However, poor thermo- and photo-stability were factors limiting the extensive use of CCC until recently. Successful realizations of DFB laser using color centers (CC) in KCl crystals were reported by Kurobori *et al.* [24] and G.C. Bjorklund [25]. Unfortunately, the laser operation required liquid nitrogen cooling of the active media down to 77K.

LiF crystals have the most suitable characteristics among alkali-haloids for the building of CC tunable lasers. LiF is less hygroscopic than other alkali-haloids, and color centers created in these crystals could be stable at room temperatures for decades. The successful realization of a room-temperature DFB laser using a LiF: F_2 color center was demonstrated by Kurobori *et al.* [26]. However, the active media degrade after 500 pumping pulses due to the poor photo-stability of F_2 color centers. Recent developments

in CCCs have made available LiF with stabilized F_2^{+3} CC (LiF:F $_2^{+3}$) crystals with high thermal- and photo-stability of doped solids and high absorption and emission cross-sections of dyes [27,28]. The F_2^{+3} CC's can be thought of as electrons trapped by two adjacent anion vacancies of crystal lattice stabilized by an additional impurity ion. The successful, stable tunable lasing at room temperature was achieved in the 0.8-1.2 μm spectral region [28]. In this manuscript we present a pulsed tunable DFB laser on a LiF:F $_2^{+3}$ crystal operating at room temperature.

The optical feedback is provided by Bragg scattering from periodic modulation of refractive index and gain of the media. The laser oscillations occur near Bragg frequency with the wavelength

$$\lambda_L = 2n\Lambda / m , \quad (1)$$

Where n is media refractive index, m is the diffraction order, and Λ is a period of perturbation. The period of perturbation, usually created by the interference of two coherent pumping beams, is given by

$$\Lambda = \lambda_p / 2 \sin(\theta) , \quad (2)$$

Where λ_p is the pumping wavelength, θ is the incident angle of the pumping beams. As one can see, the wavelength tuning could be accomplished by changing the medium refractive index and/or the grating period. In the dye laser, the solvent refraction index may be easily changed, providing tunable oscillation with a constant grating period [15]. As far as solid state laser is concerned, the oscillation wavelength tuning is usually achieved by changing the incident angle (θ) of pumping beams according to eq. (2).

The LiF crystal, grown by the Kyropulos method, was doped with LiOH, LiO $_2$, and MgF $_2$ in order to provide thermal and photo stabilization of the positive charged

CC's. A multistep technique was used in which the crystals were γ -irradiated by a ^{60}Co source in order to obtain a high concentration of F_2^{+*} centers and a low concentration of colloids and parasitic aggregate CC's. The absorption spectrum of LiF:F_2^{+*} CCC, shown in Fig. 12, revealed the absorption coefficient of the studied crystal at room temperature to be equal to $k=3.5 \text{ cm}^{-1}$ at 610 nm. On the other hand, the previous studies showed that the maximum absorption coefficient of LiF:F_2^{+*} CCC at a given wavelength could as high as 7.5 cm^{-1} .

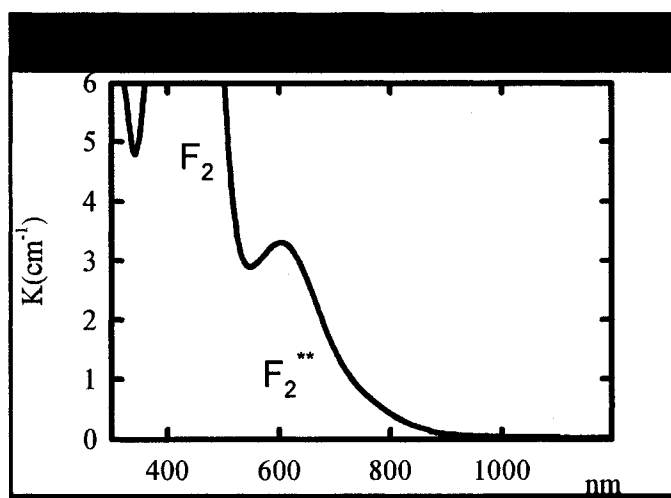


FIG. 12. Absorption spectrum of LiF:F_2^{+*} color center crystal

The experimental setup is shown in Fig. 13. The dynamic grating was created by the interference of two pumping beams of a single longitudinal mode Nd:YAG GCR 230 laser operated in the second harmonic at a wavelength of 532 nm with a 12-ns pulse duration and at a 10-Hz repetition rate. A laser beam directed through a cylindrical lens ($f=50 \text{ cm}$) was split into equal parts by a beam splitter. Two beams were finely directed to the crystal slab ($19 \text{ mm} \times 7 \text{ mm} \times 7 \text{ mm}$) by two mirrors ($R \approx 99 \%$), producing a DFB laser grating approximately 0.5 mm wide and 10 mm long. The additional feedback and

output in one direction was provided by the mirror M3. A spectrograph (Acton Research 150) with a 0.5-nm resolution and equipped with a CCD camera was used for the detection of DFB laser oscillation.

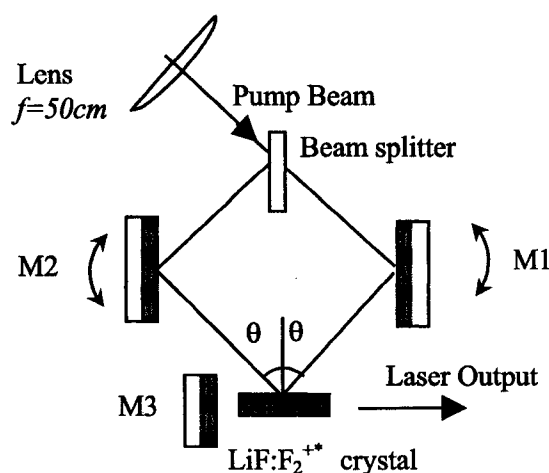


FIG. 13 Experimental setup of LiF:F_2^{+**} DFB laser.

The wavelength tuning was achieved by changing the incident angle of the pumping beams. The incident angle of the pumping beams was in the range of 50-57 degrees, which is close to the Brewster angle of the LiF crystal (54°) minimizing pumping losses. Fig. 14 shows a tuning of the DFB laser. We have obtained very narrow laser oscillation, tunable in the 882 to 962-nm range. The DFB lasing disappeared if one shoulder of the pumping was closed, and we observed a broadband radiation emission corresponding to the laser with a nonselective cavity formed by a M3 mirror and a Fresnel reflection ($\sim 4\%$) from a LiF crystal facet (curve 9). The FWHM of emission was about 20 nm, centered at 925 nm.

LiF:F_2^{+**} DFB laser output energy is shown in Fig. 15. The threshold of the DFB

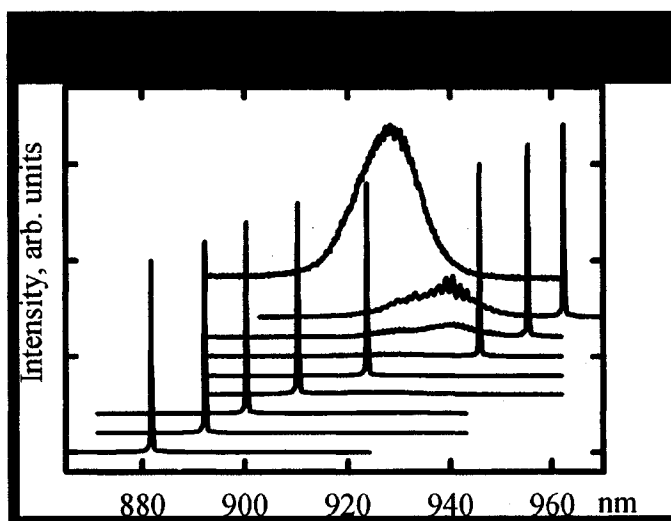


FIG. 14 Tunable operation of LiF:F_2^{+++} distributed feedback laser. The broad band at 925 nm corresponds to a laser emission with a nonselective cavity. All spectra were scaled for convenience.

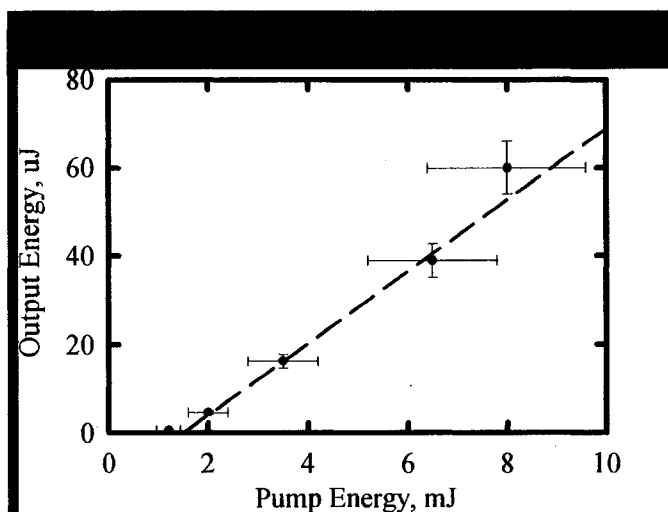


FIG. 15 The output energy of LiF:F_2^{+++} DFB laser with respect to pumping pulse energy. The time delay between pumping pulse and DFB laser oscillation was measured by a fast photodetector (Newport, 818-bb-20) with a rise time less than 200 ps.

lasing was observed at a total incident pump energy of 1.2 mJ. The conversion efficiency of 3% was achieved at 920 nm under 10 mJ pumping energy. We presume that the low conversion efficiency results from the low coupling efficiency of the Bragg scattering,

due to poor spatial coherence of the pump radiation. As one can see in Fig. 16, the rise-time of laser oscillations is a few nanoseconds. The fast rise time provides good temporal overlapping of pumping and laser emission pulses, making it promising for nonlinear wave mixing between pumping and oscillation radiation. The etalon with a 1-cm^{-1} free spectral range was used for the DFB laser oscillation linewidth measurements, as shown in Fig. 17. The FWHM of DFB laser

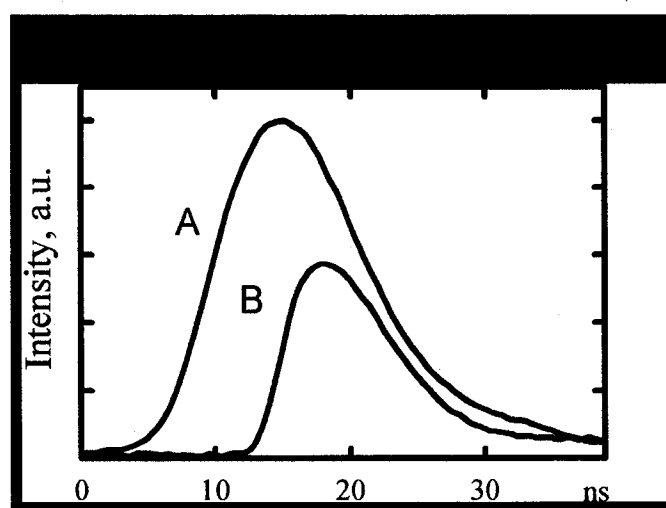


FIG. 16 Temporal delay of LiF:F_2^{+**} DFB laser emission (B) with respect to pumping pulse (A).

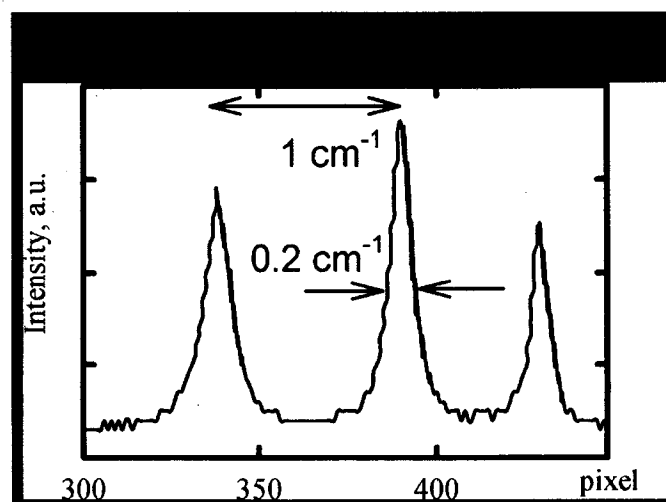


FIG. 17 LiF:F_2^{+**} DFB laser linewidth measurements.

oscillation at 920 nm was 0.2 cm^{-1} . The etalon resolution was equal to 0.1 cm^{-1} . Using a simple estimation [23] the spectral laser line ($\Delta\nu$) of the pulse DFB laser may be obtained from $\nu/\Delta\nu_{\text{cav}} \approx L/\Lambda$, where L - is interaction length. The substitution of $L=2 \text{ cm}$ and $\lambda=920 \text{ nm}$ gives a laser-linewidth $\Delta\nu \approx 0.18 \text{ cm}^{-1}$, which is in good correlation with experimental data.

In conclusion, we have obtained a tunable DFB laser operating at room temperature using LiF:F_2^{+*} CC as a gain media. Distributed feedback was based on periodic gain modulation. The incident angle of the pumping beams was close to the Brewster angle, minimizing losses. Tunable operation was archived from 882 to 962 nm, with emission linewidth less then 0.2 cm^{-1} . The maximum efficiency of 3% was achieved at 920 nm and threshold energy of 1.2 mJ.

LiF_2^{+**} tunable color center laser based on Littrow cavity

The Littrow mount scheme, or autocollimation, is the simplest dispersive laser cavity (see Fig. 18). In this cavity the diffracted beam is used for laser feedback. The zero order of the diffraction serves as cavity output. For this autocollimation regime the incidence and diffracted angles are equal ($\psi=\varphi$), and equation (1) becomes

$$2t \sin \psi = m\lambda \quad (3)$$

As one can see, the oscillation wavelength depends on the incident angle as a *sin* law. Such dependence can be easily realized and controlled by a step motor driver. The angular dispersion of a grating in this case is defined by

$$D = \frac{d\psi}{d\lambda} = \frac{2tg(\psi)}{\lambda} \quad (4)$$

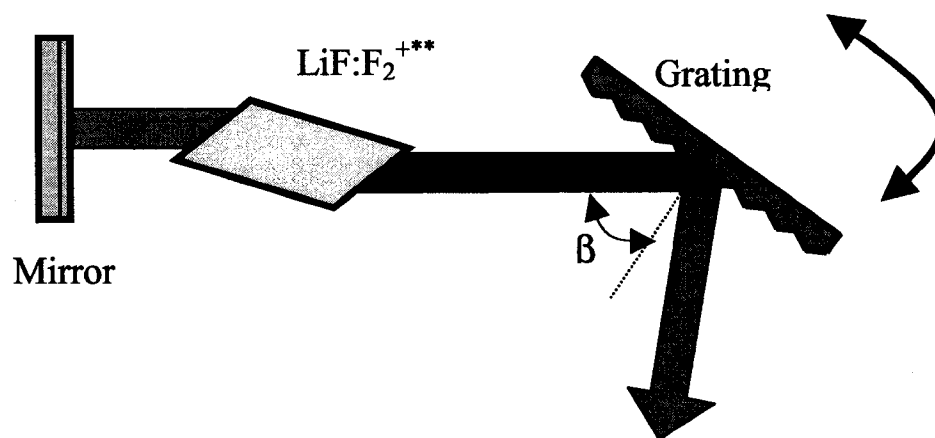


FIG. 18 Littrow cavity.

Thus the grating angular dispersion is determined only by the autocollimation angle (ψ). Angular dispersion increases with an increase in the incidence autocollimation angle. Therefore, in order to realize the narrow line oscillation, it is necessary to select the grating with the maximum autocollimation angle for the particular spectral region. Figs. 19 (a) and 19 (b) demonstrate the autocollimation angles and the wavelength dependence of angular dispersion for gratings with 1200 (1), 1600 (2), and 1800 (3) grooves/mm. One can see from Fig. 19 (a) that to tune the wavelength from 0.8 to 1.2 μm with gratings (1) to (2) it is necessary to change the incidence angles from 28 to 46 degrees and from 38 to 74 degrees, respectively. Fig. 19 (b) shows the dispersion dependence for the same gratings. As one can see, the use of 1800 and 1600 gratings instead of 1200 results in a strong increase of the angular dispersion, especially at the wavelength above 1 μm . The grating (1200 grooves/mm) can be utilized in a spectral region of 0.8-1.3 μm and features a practically constant angular dispersion of 1.3-1.9 $\text{rad}/\mu\text{m}$ over this spectral region. 1600 grooves/mm grating can be used in a spectral region of 0.8-1.23 μm and features a

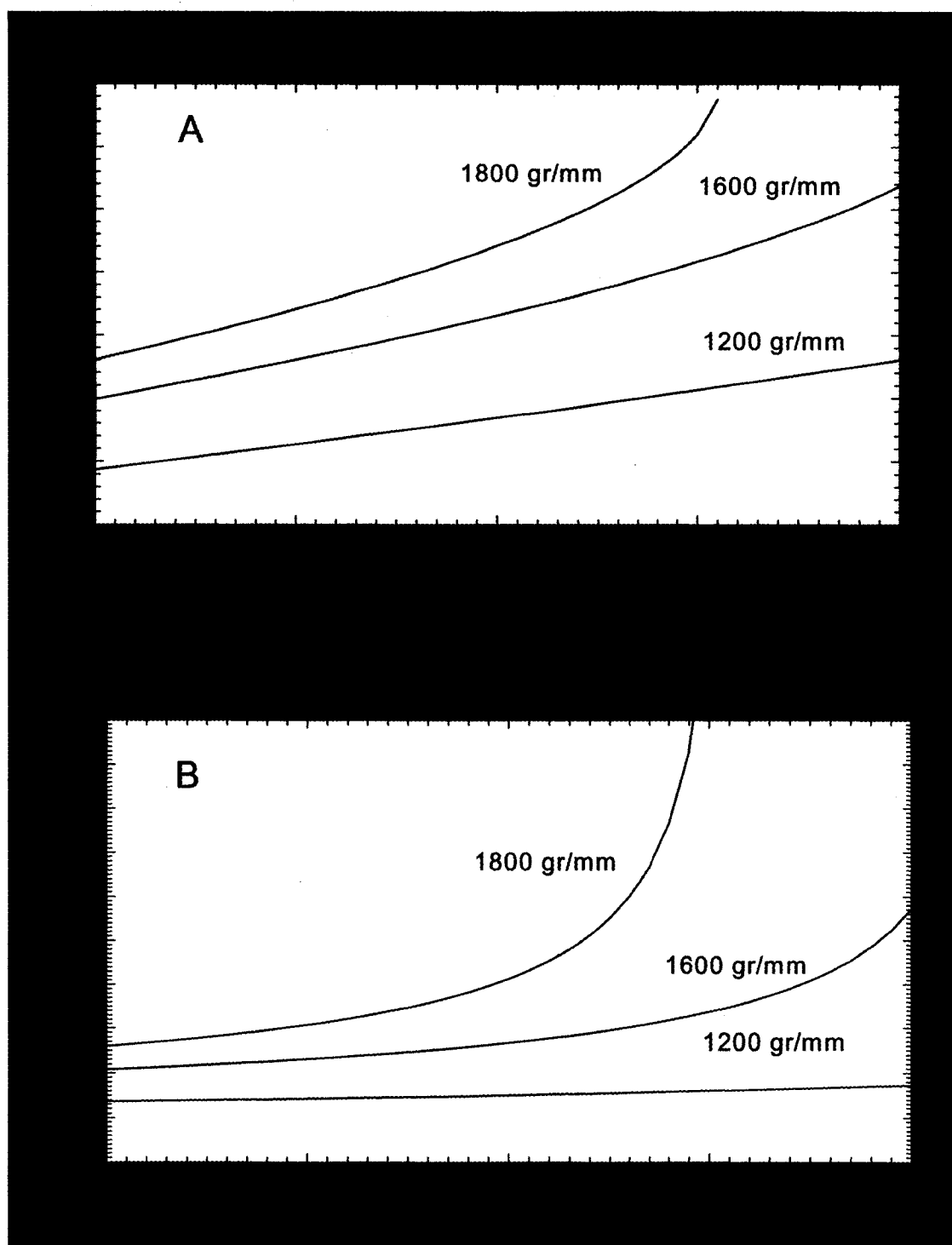


FIG. 19 The autocollimation angles (A) and the angular dispersion (B) dependences.

practically constant angular dispersion of 1.9-2.3 rad/ μm over the spectral region of 0.8-1.05 μm , as well as sharply increasing angular dispersion (from 2.3 to 10 rad/ μm) in the spectral region 1.05-1.23 μm . 1800 grooves/mm grating can be used in a spectral region of 0.8-1.09 μm and features practically constant angular dispersion of 2.3-3 rad/ μm . In our latest studies, we tested the Littrow cavity with an additional dichroic mirror and an intracavity telescope, as shown in Fig. 20. This setup provides a double pass of the pump radiation through the active element, with a corresponding increase of absorbed pump radiation and a pure longitudinal excitation with a good collinear overlapping of the pump and mode volumes, resulting in better efficiency of generation overall. A double pass of the pump radiation through the LiF crystal, in combination with the tilted mirror and a high threshold at the wavelengths of the pump radiation, ensures effective grating protection against the pump laser beam. The cavity depicted in Fig. 20 can be of three types: (a) Without telescope and etalon, linewidth is expected to be $\sim 2 \text{ cm}^{-1}$; (b) With the additional telescope. Introduction of the 10x telescope and utilization of the 1600 grooves/mm grating will provide resolving power 48000 for the 30 mm illuminated width of the grating that corresponds to a single-pass resolution of $\Delta\lambda \sim 0.2 \text{ cm}^{-1}$; and (c) With additional telescope and etalon Fabri-Perot, linewidth of 0.1 cm^{-1} can be achieved. Multiple roundtrips of the lasing radiation in this cavity may result in further line narrowing up to the regime of single-frequency generation.

We tested the spectral output of the LiF laser based on a 29-cm-long Littrow cavity (type 2) with 3x intracavity telescope and 1200 grooves/mm grating without additional intracavity etalon. The interference fringe pattern, measured with a solid state Fabri-Perot etalon (free spectral range $\Delta\nu = 1 \text{ cm}^{-1}$), is depicted in Fig. 21. The measured

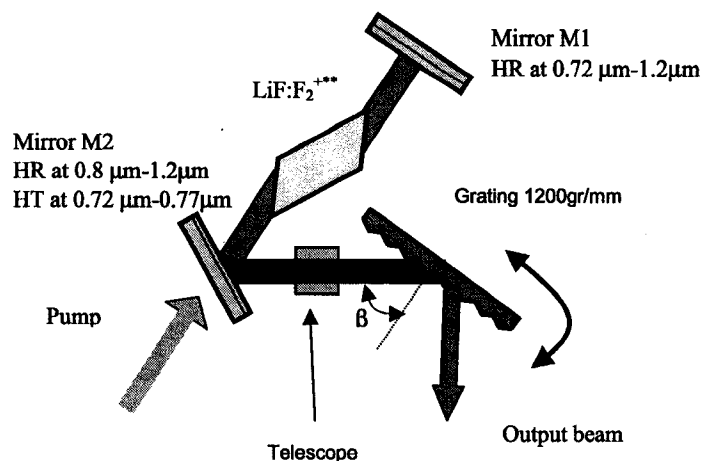


FIG. 20 Double pump pass, Littrow scheme of the LiF:F_2^{+**} laser with intracavity telescope (3x).

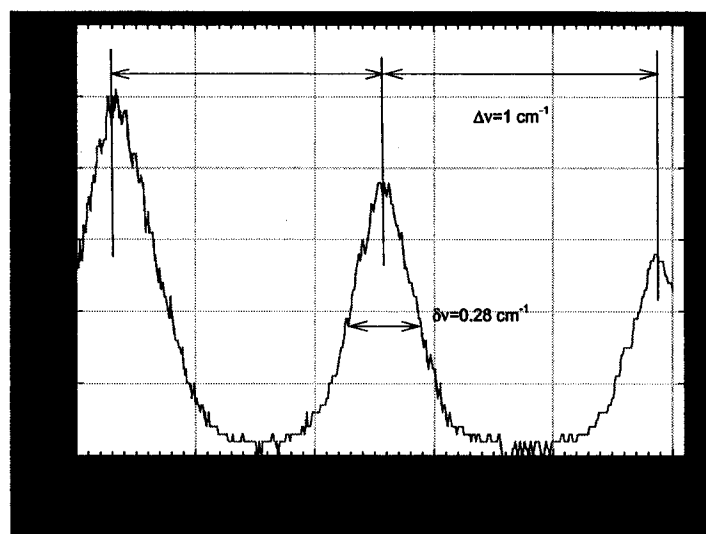


FIG. 21 Interference fringe pattern of spectral output of LiF laser based on 29 cm Littrow resonator with intracavity 3x telescope measured with F-P etalon ($\text{FSR}=1 \text{ cm}^{-1}$).

lasing linewidth was about 0.27 cm^{-1} . Hence, this scheme, with an intracavity telescope having a very simple tuning means (grating rotation), provides spectral linewidth of the output radiation comparable with the output of the LiF laser based on a Littrow resonator with intracavity etalon.

PRACTICAL APPLICATIONS OF LASER SPECTROSCOPY METHODS IN BIOMEDICAL RESEARCH AND ENVIRONMENTAL MONITORING

Laser spectroscopy study of superoxide dismutase (SOD)

Fluorescence assay for monitoring Zn-deficient superoxide dismutase in vitro

Introduction. Amyotrophic lateral sclerosis (ALS) is a neurodegenerative disease which occurs due to the death of motor neurons. Survival after diagnosis is typically less than 5 years due to resulting progressive paralysis and atrophy of all voluntary muscles, including muscles of mastication, swallowing, and breathing. There is no effective treatment.

The only known cause of ALS is mutations to SOD1, which have been found in roughly 2% of ALS cases. Nevertheless, there are no clinical or histopathological differences between SOD1-mediated and non-SOD1-mediated disease. This fact leads many investigators to conclude that all forms of ALS may have a common etiology, based on SOD1 mutations.

The proposed hypothesis explains how more than 90 different single amino acid mutations can all result in the same toxic phenotype, why motor neurons are particularly susceptible, and how wild-type SOD1 can become toxic in the same manner as mutant enzymes and thereby cause all forms of ALS. It states that the balance between normal and toxic functioning of SOD1 hinges upon whether zinc is bound in the active site of the enzyme. Thus, the capability to identify and quantify zinc-deficient SOD1 is strategically important for further characterization of SOD1-mediated toxicity in ALS. The common function of SOD1 is to remove the oxygen radical superoxide ($O_2^{\cdot -}$)

and therefore limit superoxide-dependent toxicity. SOD1 is present in cells at a very high concentration ($\geq 10 \mu\text{M}$ [29]) relative to most enzymes. The active site of SOD1 has copper ion and zinc ion bound by a common histidyn residue. The copper ion is essential for enzyme activity. It undergoes a one-electron reduction and reoxidation during one complete catalytic cycle. In contrary, the zinc ion does not redox cycle and has been considered to serve a mainly structural role.

The mechanism by which SOD1 mutants cause ALS remains unclear. Zinc-binding affinity is substantially decreased in mutant enzymes. The mutations alter the protein's conformation and deoptimize the zinc-binding ligands [30,31,32]. These findings lead to one of the key hypotheses. In the beginning, it was not clear how a change in zinc-binding affinity could translate into a toxic gained function. It was found recently that zinc acts to maintain a rigid and tightly constrained active site in such a way that compounds larger than superoxide are excluded from interacting with the copper ion. In other words, zinc functions to help maintain enzyme specificity to superoxide and avoid promiscuous reactions with other low molecular weight reductants and oxidants.

If zinc is absent, the other reductants such as ascorbic acid, urate, NADH, and glutathione are capable of entering the active site and reducing Cu^{2+} to Cu^{1+} [33]. The effect of this abnormal copper reduction is to permit the enzyme to transfer electrons from cellular antioxidants to molecular oxygen and thereby generate superoxide, i.e., to run in reverse. However, the rate of this reverse reaction is less than the rate of the competing forward reaction (rate constant for superoxide reacting with C(I)-SOD1 is $2 \times 10^9 \text{ M}^{-1}\text{s}^{-1}$), hence the equilibrium disfavors the production and release of free superoxide from Cu^{1+} -SOD1 and oxygen. On the other hand, superoxide reacts with nitric oxide (NO) eight times faster than it reacts with SOD1, and the reaction of superoxide and NO

produces the potent cytotoxin and nitrating agent peroxynitrite. Nitric oxide is a small, uncharged molecule that can readily enter the active site of SOD1, shifting the equilibrium in favor of superoxide production from Cu(1)-SOD1 and oxygen; the net result is a "peroxynitrite synthase" activity (of zinc-deficient SOD1) that is largely driven by the concentration of NO.

Zinc-deficient SOD1 can abnormally utilize cellular antioxidants, oxygen, and NO to catalytically produce peroxynitrite. Even a small fraction of the zinc-deficient SOD1 would result in continuous peroxynitrite production. The various enzyme mutations may serve simply to increase the probability that the mutants would exist in a zinc-deficient state. Thus, all single-amino-acid mutations associated with ALS could result in the formation of the same toxic phenotype via effects on zinc-binding affinity. The NO-dependent, apoptotic cell death has been initiated by introducing zinc-deficient SOD1 into primary motor neurons in culture [33]. Even wild-type SOD1 have been found to be toxic when deficient in zinc. This fact is the additional evidence that toxicity is a function of the absence of zinc and not the mutation by itself. This finding suggests the exciting possibility that all forms of ALS can be explained on the basis of a gained function for SOD1, since one need only upregulate the biosynthesis of other zinc-binding proteins to out-compete apo wild-type SOD1 for zinc and result in the formation of a zinc-deficient, wild-type enzyme. The increased levels of both free and protein-bound nitrotyrosine in the lower motor neurons of transgenic mice and in both the upper and lower motor neurons in individuals with ALS is the only evidence of a role for nitric oxide and peroxynitrite in ALS [29,34-36]. The additional support for this hypothesis in the form of actual measurement of zinc-deficient SOD1 *in situ* is required. The crucial problem is due to changes in metallation states upon cell lysis. Zinc-deficient SOD1 readily rebinds zinc

and exist in a zinc-deficient form only because of dynamic competition with other zinc-binding proteins for available cytosolic zinc. A technique for measuring zinc-deficient SOD1 in intact cells would evade the problems associated with changes in metallation state upon cell lysis.

Direct measurement of zinc-deficient SOD1 *in situ* would test this hypothesis as well as provide a way to monitor the effects of any treatments aimed at decreasing the levels of zinc-deficient enzymes within neurons. Two properties of zinc-deficient SOD1 that serve as the basis for a sensitive and highly selective fluorescence-based assay have been identified. Zinc-deficient SOD1 is different from the zinc-containing enzyme in two important respects. First, it can be rapidly reduced by reductants such as ascorbate, and second, it reacts with the specific copper chelator bathocuproine disulfonate (BCDS). The reaction of BCDS with zinc-deficient Cu^{1+} -SOD1 leads to the formation of a complex with maximum of light absorption at 482 nm. The excitation of this complex results in a fluorescent signal in the region of 680 to 750 nm. In addition, reaction of zinc-deficient SOD1 with BCDS quenches the intrinsic fluorescence of BCDS. We could not distinguish the difference between BCDS complexes with free Cu^{1+} and Cu^{1+} -SOD1, since the fluorescence characteristics of the BCDS/SOD1 complex are essentially identical to those of free Cu^{1+} -BCDS. However, Cu^{1+} ions do not exist in a free form in cells and, even if free Cu were present, their reaction with BCDS would not be inhibited by pretreatment with zinc as would the reaction of BCDS with zinc-deficient SOD1. The existence of zinc-inhibitable fluorescence of a BCDS- Cu^{1+} complex would thus indicate the existence of zinc-deficient SOD1 in cells.

Material and Methods. D124N (aspartate replaced by asparagine at position 124) is a site-directed human SOD1 mutant. It has been shown to bind zinc with much less affinity than does wild-type SOD1 [37]. D124N binds zinc poorly even in the presence of free zinc and is, therefore, used as a model enzyme to investigate the spectral properties of the zinc-deficient enzyme. Recombinant D124N SOD1 was prepared by expressing the mutated protein in *E. coli* as described previously [31,32].

CuSO₄ at the appropriate concentrations was used as a source of free Cu. CuSO₄ and zinc-deficient SOD1 were reduced by ascorbic acid followed by addition of BCDS. A 100-mM potassium phosphate buffer (pH 7.2) was used to maintain pH of the solution.

A Shimadzu UV-VIS-near-IR spectrophotometer was used to measure absorption spectra. Frequency doubled radiation of an LiF:F₂⁺⁺⁺ tunable laser at 480 nm was used for fluorescence excitation. The average power of radiation was about 10 mW at a repetition rate of 26 Hz and a 50-ns pump pulse duration. A spectrograph (Acton Research 150) equipped with a thermo-electrical cooled CCD camera was used for fluorescence detection.

Absorption. The reduced CuSO₄ or zinc-deficient SOD1 form a colored complex with specific absorption band at 482 nm and an FWHM of about 80 nm. The absorption spectra are shown in Figs. 22 (a) and 22 (b). BCDS forms a 2:1 tetrahedral complexes with free Cu¹⁺. The absorption spectrum of (BCDS)₂-Cu¹⁺ is identical to that obtained with BCDS and zinc-deficient Cu¹⁺-SOD1. The BCDS has no absorption at 482 nm (Fig. 22c). Thus, fluorescence of BCDA should not be resonantly excited at the same wavelength as (BCDS)₂-Cu¹⁺ complexes.

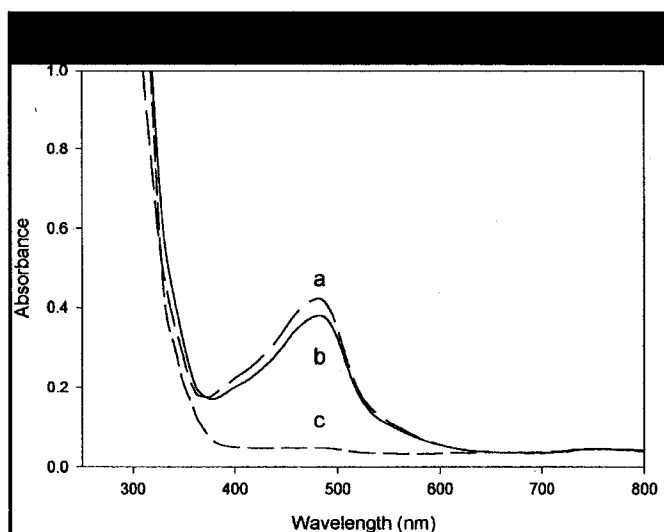


FIG. 22. Absorption spectra of (a) mixture of D124N SOD1 0.8 mg/mL, BCDS 0.1 mM, and ascorbic acid 0.05 mM; (b) mixture of 0.05 mM CuSO_4 , 0.1 mM BCDS, and 0.05 mM ascorbic acid; and (c) mixture of metal replete wild-type SOD1 (0.8 mg/ml), 0.1 mM BCDS, and 0.05 mM ascorbic acid, in 100 mM potassium phosphate buffer.

The absorption spectra indicate that BCDS does not react with metal replete (i.e., zinc- and copper-containing) wild-type SOD1 (Fig. 22c.) It was determined previously that the reaction of BCDS with the active-site copper atom is prevented by the presence of enzyme-bound zinc; no reaction with BCDS is seen, even when the copper is reduced by ascorbate prior to adding BCDS.

Fluorescence. BCDS has a relatively strong fluorescence emission if excited at 482 nm, as shown in Fig. 23, regardless of weak absorption at this wavelength. $(\text{BCDS})_2\text{-Cu}^{1+}$ complexes have a fluorescence band centered at 734 nm, with a FWHM of 150 nm. The formation of $(\text{BCDS})_2\text{-Cu}^{1+}$ complexes fluorescence band was accompanied by fluorescence quenching of free BCDS. The free BCDS fluorescence was completely quenched once the copper concentration reached a two-fold threshold, and we observed

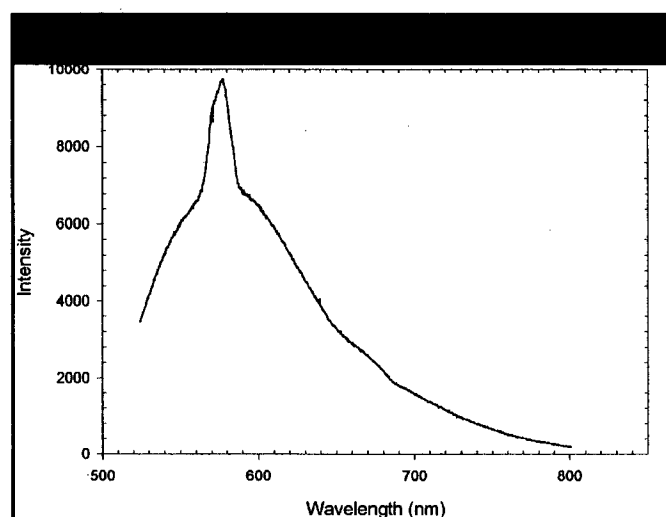


FIG. 23. Fluorescence spectrum of BCDS in 100 mM potassium phosphate buffer excited at 482 nm. The relatively narrow band at 576 nm corresponds to the Raman scattering of water.

the fluorescence of the $(\text{BCDS})_2\text{-Cu}^{1+}$ complex only. The spectrum of the $(\text{BCDS})_2\text{-Cu}^{1+}$ complexes fluorescence is shown in Fig. 24. The emission spectra of BCDS complexes with D124N (zinc-deficient) SOD1 showed the same features. On the contrary, the fluorescence of BCDS was not completely quenched upon complexation with zinc-deficient SOD1. The BCDS fluorescence was not completely quenched even at a concentration of zinc-deficient SOD1 several fold higher comparing to the BCDS concentration. The spectrum shown in Fig. 25 is a superposition of the fluorescence signal of BCDS, the $(\text{BCDS})_2\text{-Cu}^{1+}$ complex, and Raman scattering of water at 3400 cm^{-1} (576 nm). The fluorescence of the $(\text{BCDS})_2\text{-Cu}^{1+}$ complex strongly overlaps with the fluorescence of BCDS and could not be simply resolved in the spectral region from 650 nm to 750 nm. The deconvolution of the spectrum is required in order to distinguish the distinct fluorescence of the $(\text{BCDS})_2\text{-Cu}^{1+}$ complex from the fluorescence of BCDS. The fluorescence signal was approximated as a set of bands with a Gaussian shape. The deconvoluted BCDS

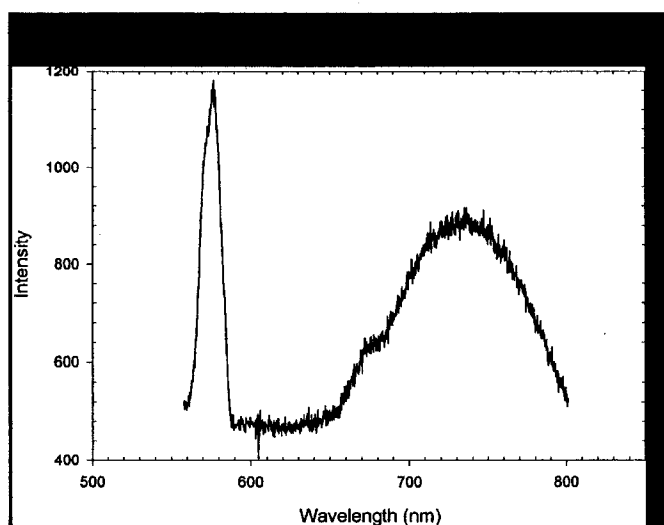


FIG. 24. Fluorescence spectrum of the BCDS complex with free Cu^{1+} in 100 mM potassium phosphate buffer excited at 482 nm. CuSO_4 was present at a concentration of 0.9 mM, BCDS at 0.3 mM, and ascorbic acid at 2.5 mM. The narrow line at 576 nm corresponds to the Raman scattering of water.

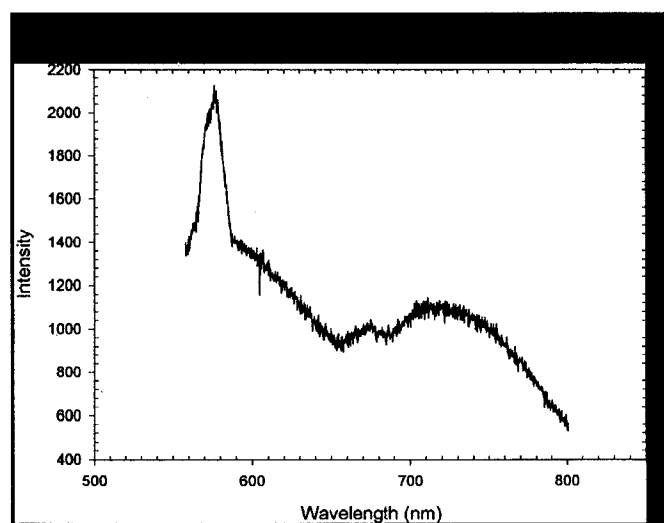


FIG. 25. Fluorescence spectrum of the BCDS complexes with D124N (zinc-deficient) SOD1 excited at 482 nm. D124N SOD1 was present at a concentration of 0.075 mM, BCDS at 0.3 mM, and ascorbic acid at 2.5 mM in 100 mM potassium phosphate buffer pH 7.2. The narrow line at 576 nm corresponds to the Raman scattering of water.

fluorescence spectra is shown in Fig. 26. The bands at 574 nm and 662 nm correspond to the fluorescence of BCDS, while the narrow 576 nm band corresponds to the Raman scattering of a water at 3400 cm^{-1} . The addition of an excessive amount of Cu ions led to

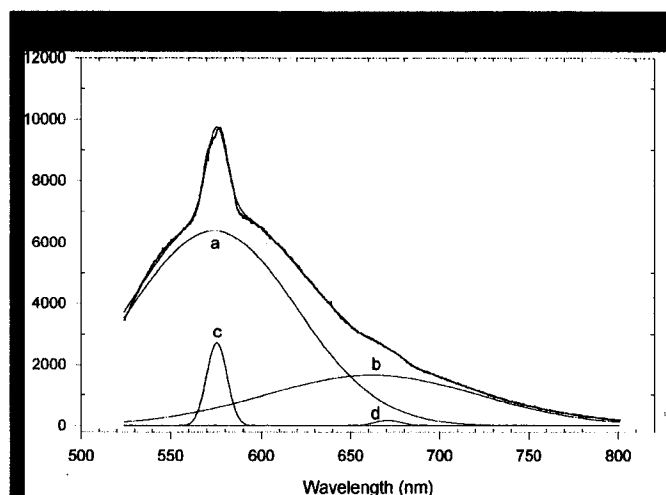


FIG. 26. Deconvoluted spectrum of BCDS fluorescence. Bands a) and b) centered at 573.98 nm and 662.18 correspond to BCDS fluorescence, c) band centered at 576 nm corresponds to Raman scattering of water, and d) 671-nm band is an artifact which is present in all spectra.

the complete quenching of BCDS fluorescence and the appearance of a new fluorescence band at 734.7 nm corresponding to the fluorescence of $(\text{BCDS})_2\text{-Cu}^{1+}$ complexes. The deconvoluted spectrum of $(\text{BCDS})_2\text{-Cu}^{1+}$ complexes fluorescence is shown in Fig. 27.

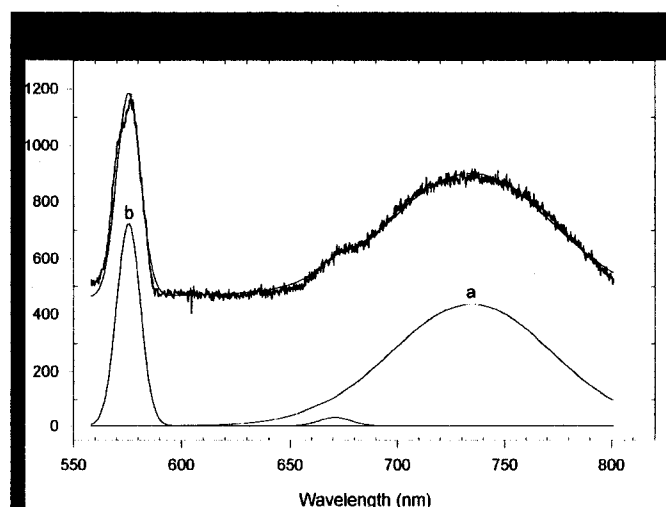


FIG. 27. Deconvoluted spectrum of $(\text{BCDS})_2\text{-Cu}^{1+}$ complexes fluorescence. Band a) centered at 734.67 nm corresponds to fluorescence of $(\text{BCDS})_2\text{-Cu}^{1+}$; b) 576-nm band corresponds to Raman scattering of water.

The intensity of each fluorescence band can be precisely determined by a fitting procedure if one knows the exact position and FWHM of each band. The results of this procedure are shown in Fig. 28. The calculated curve fits the experimental data with an R value better than 0.99 in all cases. Data acquired from the fitting procedure represent the actual fluorescence intensity of the BCDS complexes with zinc-deficient SOD1. Finally, the calibration curve can be found using fluorescence intensity values determined by fitting procedure. The calibration curve is shown in Fig. 29.

The BCDS fluorescence band at 573.98 nm and the fluorescence band of BCDS complexes with zinc-deficient SOD1 at 735 nm are well separated and, therefore, the ratio method could be used for quantitative measurements, as well.

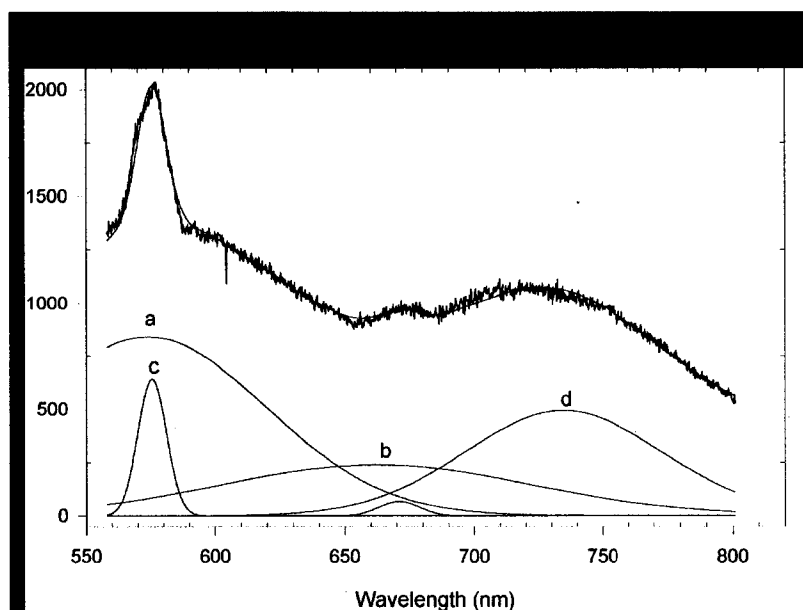


FIG. 28. Deconvoluted spectrum of the BCDS/ Cu^{1+} -SOD1 (D124N mutant) complexes fluorescence. D124N SOD1 was present at a concentration of 0.075 mM, BCDS at 0.3 mM, and ascorbic acid at 2.5 mM in 100 mM potassium phosphate buffer pH 7.2. Bands a) and b) centered at 573.98 nm and 662.18 correspond to BCDS fluorescence, band c) at 576 nm corresponds to Raman scattering of water, and d) 734.67 nm corresponds to fluorescence of the BCDS/ Cu^{1+} -SOD1 (D124N mutant) complexes.

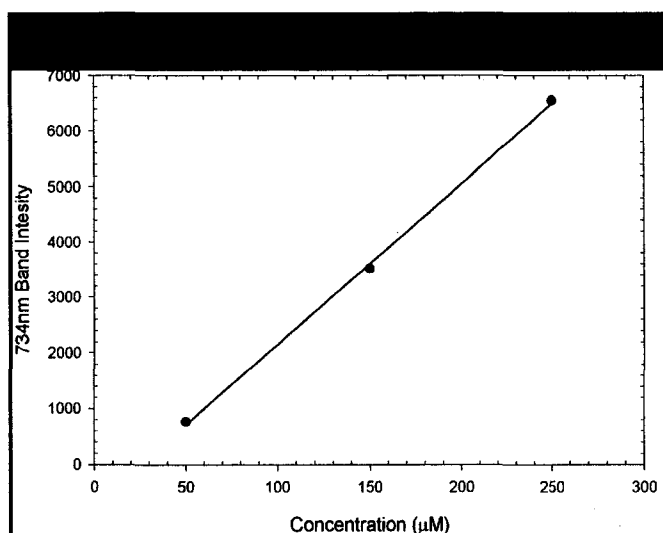


FIG. 29. Intensity of the 734 nm fluorescence band of the BCDS/Cu¹⁺-SOD1 (D124N mutant) complexes as a function of concentration.

Conclusions. It was demonstrated that complexes of BCDS with Cu¹⁺ and zinc-deficient SOD1 have a characteristic fluorescence band at 734 nm with a FWHM of 150 nm under resonance excitation at 482 nm. This fluorescence band could be used for qualitative and quantitative determination of zinc-deficient SOD1 in cells by means of fluorescence confocal microscopy (FCM).

The smallest concentration of zinc-deficient SOD1 detected in our experiments was 50 µM. That is about ten times higher than physiological concentrations of SOD1 in cells. However, preliminary estimations of the detection limit of a microscope-based system equipped with a liquid nitrogen cooled CCD camera showed that physiological concentrations of SOD1 could be measured with a reasonable signal-to-noise ratio. Detailed calculations of the detection limit of microRaman/Fluorescence imaging system Dilor XY, which we plan to use for detection of SOD1 in cell culture, can be found in the Appendix. Therefore, we expect that the confocal microscope should provide the required sensitivity for detection of zinc-deficient SOD1 in cell culture. This method will be fur-

ther refined in testing the zinc-deficient SOD1 hypothesis in ALS. Measurement of zinc-deficient SOD1 *in situ* (using fluorescent confocal microscopy) would provide additional support for the fundamental hypothesis regarding the toxic form of SOD1 mutants in ALS and provide a way to monitor treatments designed to reduce the levels of the zinc-deficient enzyme.

We assume that the BCDS-D124N SOD1 complex did not exist at the time measurements were made due to the similarity of the absorption and fluorescence spectra of BCDS complexes and free Cu^{1+} . Nevertheless, quenching of the intrinsic BCDS fluorescence by free Cu^{1+} is two-fold more efficient than an equal concentration of zinc-deficient SOD1, which is consistent with a 1:1 complex of BCDS with in active site Cu^{1+} , compared to a 2:1 complex of BCDS with free Cu^{1+} . Therefore, the nature of the BCDS/SOD1 complex remains unresolved.

Recent studies showed that copper almost doesn't exist in cells in a free form. Mechanisms have evolved to prevent free copper from existing within cells since it is strongly pro-oxidant and causes oxidative injury to cells. The estimated free copper concentration is about one atom per cell [38]. Thus, the formation of a fluorescent complex upon addition of BCDS to cells would likely indicate the presence of zinc-deficient SOD1. There is a possibility that BCDS would extract the copper from other copper-binding proteins, but it is most unlikely that such copper extraction would be inhibitable by pretreatment with zinc. Thus, a zinc-inhibitable formation of a fluorescent BCDS complex would strongly suggest the presence of zinc-deficient SOD1 in cells.

Surface Enhanced Raman (SERS) study of superoxide dismutase (SOD)

Introduction. In spite of the high sensitivity of fluorescence measurements, this method has a serious drawback, due to the nature of the fluorescence. The fluorescence bands are relatively broad, about 50 to 100 nm, and thus spectral resolution is limited. As we have seen in a previous section, the fluorescence of BSDA-Cu¹⁺ complexes overlaps with BSDA fluorescence and could not be resolved without deconvolution. This procedure seems to be difficult to perform in the case of confocal fluorescence microscopy measurements. Moreover, it does not allow one to distinguish the difference between free Cu¹⁺ and zinc-deficient SOD. One of the reasons is that fluorescence spectroscopy does not carry information about the chemical specificity of the sample.

The technique that has a required spectroscopic selectivity is Raman spectroscopy. It has been used for a long time for analytical purposes due to its unique capability of chemical group identification. The widths of Raman lines are relatively narrow, usually less than 1 nm, so they could be easily resolved, even for complex samples, and used for multielement analysis.

The Raman effect is the inelastic scattering of incident radiation. The scattered light is shifted in frequency by the energy of the characteristic vibration of molecules. The main advantage of Raman spectroscopy is the capability to provide rich information about molecular structure. However, conventional Raman spectroscopy has a significant drawback: an extremely small, usually about 10^{-30} -cm², cross-section of Raman scattering. Such a small cross-section requires a large number of molecules and/or high intensity of incident radiation, resulting in possible damage to the biological sample.

A new phenomenon was observed in 1974 by Fleischmann, Hendra, and McQuillan [39]. They detected a very intense Raman spectra of pyridine molecules adsorbed on

the silver surface of an electrochemical cell. This phenomenon was called Surface Enhanced Raman Scattering (SERS). SERS attracted considerable attention from researchers and, in a few years, SERS spectra were reported for many molecules.

The enhancement of Raman scattering occurs if a molecule is in a close affinity to or attached to the metallic nanostructures, which are called SERS active substrates. In other words, SERS active substrates are different metallic structures with a size range from dozens to hundreds of nanometers. The most common SERS active substrates are colloidal silver or gold nanoparticles 50 to 150 nm in size, silver or gold electrodes, and films prepared by cold deposition of these metals or electron-beam lithography.

The enhancement mechanisms are divided into electromagnetic and chemical. The electromagnetic mechanism is due to the interaction of a molecule with an electromagnetic field near the metallic surface, also called surface plasmon resonance, and has a spatial range of about 10 nm. The second type of enhancement is due to the formation of molecular metal complexes, which lead to the electronic coupling between molecules and metal. The spatial range of chemical enhancement is about 1 nm.

There are several theoretical descriptions of phenomenon available based on quantum and classical approaches. A detailed overview and discussion of the advantages and drawbacks of each approach will be given later. Theoretical predictions based on surface plasmon resonance theory give enhancement on the order of 10^6 - 10^8 for isolated silver or gold particles [40-46]. However, chemical mechanism enhancement could be much higher in this case. The highest enhancement was observed for Rhodamine 6G molecules adsorbed on colloidal silver particles and was estimated to be on the order of 10^{14} - 10^{15} [47]. The cross-section of Raman scattering was about 10^{-16} cm². A Raman signal was observed from a single Rhodamine 6G molecule. The observation of an extremely high

cross-section of Raman scattering was reported for several other substances (for review see Ref. 48).

Metal Colloids as a SERS active substrate. Metal colloids are used as markers for cell surfaces and intracellular components in microscopic observations. They are ideal for SERS measurements of intracellular components as well. SERS-active surfaces such as films or electrodes are not applicable, due to short enhancement range. An additional advantage of colloids is a simple experimental pretreatment procedure and the possibility of SERS measurements in conventional liquid cells.

The enhancement factor is strongly dependent on the size and shape of metal nanoparticles. Nie and Emory found an enhancement factor on the order of 10^{14} - 10^{15} for the Rhodamin 6G molecules adsorbed on single silver particles [47]. They found that only small numbers of particles exhibit high enhancement efficiency. They called them "hot particles." The atomic force microscopy showed that hot particles were isolated silver particles of about 120 nm. In a more detailed study, Emory *et al.* found that different particles are hot for a special wavelength [49], and that only a few particles have an optimum size and shape in heterogeneous collection for a given excitation wavelength. However, many SERS experiments show that colloidal particles should be preaggregated to become SERS active. During the preaggregation procedure, the aggregates or clusters (consisting of several to dozens of single nanoparticles) are forming. In general, the excitation is not distributed uniformly over the entire cluster, but localized in so-called "hot" areas.

Potential of SERS in Biology and Medicine. The effective cross-section of SERS transitions and fluorescence are comparable and therefore has the potential to combine the sensitivity of fluorescence and the analytical capabilities of Raman spectroscopy. High cross-sections of SERS allow the use of low-intensity laser radiation, usually about 10 mW, and concentrations of biomolecules comparable with physiological values. Moreover, SERS has additional selectivity in comparison to conventional Raman spectroscopy and resonance Raman spectroscopy. Raman scattering of chemical groups that are close to the metal surface will be enhanced only due to the short range of SERS. Therefore, SERS provides additional information about molecular structure. That makes SERS a powerful, noninvasive analytical technique for biomedical applications.

An example is a study by Nabiev *et al.* [50]. The ability to detect a SERS signal from a very dilute (up to 10^{-10} M) solution of doxorubicin (DOX) and 4'-O-tetrahydropyranyl-adriamycin, as well as their complexes, with targets *in vitro* and *in vivo*, has been demonstrated. SERS spectra were obtained from a cell population as well as from single living erythroleukaemic K562 cell treated with doxorubicin.

A great number of biomolecules, such as lipids, DNA, mono and polynucleotides, amino acids, and proteins, were studied by means of SERS *in vitro* [50-52]. The SERS of the single molecule of adenine was reported, and the possibility of using SERS in detection of DNA sequencing is discussed in Ref. 48. The SERS of a single hemoglobin molecule on silver nanoparticles [53] and a single Tyrosine molecule on aggregated silver colloids [54] have been reported recently.

Detection of zinc-deficient superoxide dismutase with SERS and comparison with resonance Raman spectroscopy measurements. The metal coordination of histidine residues in the active site of native enzyme (oxidized wild-type SOD) is available from the Protein Data Bank, identification code 2SOD. The Cu^{2+} is bound to the four histidines (His44, 46, 61 and 118), forming a tetragonal structure, while Zn^{2+} is bound to the three histidines (His61, 69, and 78) and one aspartate ligand, forming a tetrahedral structure. One histidine (His-61) is bound to both the Cu and Zn atoms via an imidazole ring. The imidazol bridge plays an important role in the electric properties of Cu tuning its catalytic activity.

The X-ray crystallography suggested that the imadazol bridge is preserved in the reduced state of Cu [55]. However, other spectroscopic studies, including subsequent X-ray absorbtion [56,57] and resonance Raman spectroscopy suggest that the bridge is broken upon Cu reduction, and that the N_τ atom of the imidasol ring bears proton instead [58,59].

The first attempts to study SOD by means of RRS was done in 1989 by Hashimoto *et al.* [60], but more comprehensive studies appeared only recently [58,57]. Here we will give a brief overview of those results.

Raman bands at 986, 1050, 1282/1292, and 1564 cm^{-1} in resonance Raman spectra were attributed to the ring modes of the His61 imidazolate group, which bridges Cu^{2+} and Zn^{2+} ions. These bands disappeared when metals ions were removed (apoSOD). They also disappeared when Cu was reduced with dithionite indicating the absence of an imidazolate bridge in reduced SOD. The new band appeared when SOD was incubated with D_2O , which is attributed to ring modes of imidazole ligand bound to the Zn and Cu ions. These modes became enhanced as a result of H/D exchange at imidazole N atoms oppo-

site to the metal ion. The doublet at 1282/1292 cm^{-1} remains unaltered, since imidazolate has no exchangeable protons. New bands appear at 1360, 1388, 1396, and 1406 cm^{-1} . To investigate the nature of these bands the following experiment were done:

- (1) SOD was prepared with the zinc site empty [Cu_2E_2], (2) the Cu site empty [Zn_2E_2],
- (3) both sites filled with Cu [Cu_2Cu_2], and (4) both sites filled with Zn [Zn_2Zn_2].

When Cu was removed, 1050, 1360, and 1396 cm^{-1} remained, but they disappeared when Zn was removed. Therefore, these bands were assigned to Zn-imidazol modes. On the other hand, 986, 1388, and 1406 cm^{-1} are more prominent when Zn is removed and have altered intensities for Cu^{1+} in comparison to Cu^{2+} .

Consequently these bands were assigned to the Cu-imidazol modes. The doublet 1282/1292 cm^{-1} was absent upon removal of one or both metals. Inserting Cu instead Zn partially restored doublet 1282/1292 cm^{-1} , and spectra show increase of 1388- and 1406- cm^{-1} bands intensity at expense of the 1396- cm^{-1} band. Bovine SOD has two histidines residues, which are not ligands to the metals. At pD5.1 they are partially protonated and contribute to the 1409 cm^{-1} band.

The metal-bound ImD bands were studied previously by Hashimoto *et al.* [59] on Zn^{2+} -(His)₂, Cu^{2+} -GluHis, and Cu^{2+} - β AlaHis, excited at 240 nm. They found that a strong band appears at 1390 for Zn^{2+} -(His)₂ and Cu^{2+} -GluHis, which contain N_π -lidated ImD, so they concluded that a 1390- cm^{-1} band may be used as a marker for N_π -metal ligation. On the other hand, Cu^{2+} - β AlaHis has a strong band at 1352 cm^{-1} , which may be used as a marker for N_τ -metal ligation.

Resonance Raman spectroscopy could not be performed *in vivo*, since it requires UV light for excitation and since concentrations of molecules should be higher than

physiological, but it provides very useful information about vibration modes of molecules. The affinity of molecules to the metal surface very seldom substantially changes molecular vibration frequencies. Therefore, information obtained by resonance Raman spectroscopy could be compared with data from SERS experiments and used as a control.

Experimental setup. The experimental setup is shown in Fig. 30. We used a standard 90 degrees collection scheme. Radiation of the second harmonic of a Nd:YAG laser at 532 nm (CrystaLaser) was focused into the sample. The power of laser radiation was 15mW in all our measurements. A beam caustic was imaged on the entrance slit of the spectrograph (Acton Research 150). SERS spectra were collected with a thermo-electrical cooled CCD camera. We used a supernotch filter (Kaiser Optical Systems) to eliminate scattered laser radiation. Each SOD SERS spectra were accumulated for 10 min.

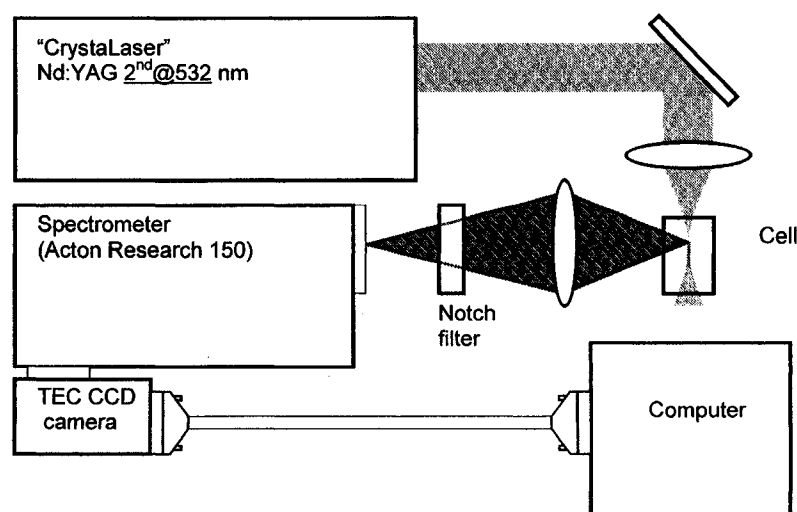


FIG. 30 Experimental setup for SOD Raman studies

Colloids preparation. Colloidal silver was prepared by reduction of silver nitrate with trisodium citrate as described by Lee and Melsel [61]. These colloids are known to have the best SERS activity. AgNO_3 (90 mg) was dissolved in 500 mL H_2O and brought to a boil. A solution of 1% sodium citrate (10 mL) was added portionwise, and the solution was boiled for another hour. The absorption spectra of colloids showed a broad band with a maximum at 408 nm due to the light scattering on metal particles (Fig. 31). The studies of citrate colloids by means of electron microscopy showed that they have a broad size distribution, with a mean diameter of about 100 nm. The formation of aggregated particles is not typical for citrate colloids; thus they are stable for several months.

Another colloid was prepared by silver nitrate reduction with NaBH_4 . A solution of 5 mM AgNO_3 (100 mL) was added portionwise to 300 mL of vigorously stirred ice-cold 2 mM NaBH_4 . The mixture was boiled for 1 h to decompose any excess of NaBH_4 . The absorption band of these colloids has a maximum at 395 nm and is narrower than the citrate one. This indicates a more narrow size distribution of particles.

Colloids were preaggregated by NaCl , KBr , or NaClO_4 prior to mixing with SOD. After preaggregation, colloids became blue in color, and absorption spectra had a wide shoulder-in-red region, indicating the formation of aggregates with a very wide size distribution.

Results. The SERS spectra of Cu,Zn SOD1 and zinc-deficient SOD1 are shown in Fig. 31. The concentration of enzymes was 0.4 mM. Spectra have an average of 500 acquisitions of 1 s each. As one can see, the zinc-deficient enzyme has a prominent band at 1384 cm^{-1} , which can be assigned to the His-Cu mode. The Raman band at 1384 cm^{-1} has

a shoulder-in-the blue region, indicating the presence of a weak band, presumably at 1349 cm^{-1} , which can be assigned to the His-Cu mode as well and corresponds to N_{π} -metal ligation. The same band can be observed in the Cu,Zn SOD1 spectrum. Weak bands in zinc-deficient enzymes around 1270-1313 can be assigned to N_{π} -ligated Im modes as well. These bands are weak, since there are three N_{τ} -ligated and one N_{π} -ligated imidazole(s) in the zinc-deficient enzyme. In contrary, Cu,Zn SOD1 has three N_{τ} -ligated and four N_{π} -ligated imidazoles. Thus, Raman bands around 1270-1313 cm^{-1} are stronger, as shown in Fig. 31b. Additionally, these bands could be assigned to the Zn-His-Cu mode. The Raman band at 1384 cm^{-1} is absent in the Cu,Zn SOD1 spectrum (Fig. 31b). However, there are bands at 1349 cm^{-1} (N_{π} -metal ligation), 1366 cm^{-1} (His-Zn mode), and 1395 cm^{-1} (His-Zn mode).

The smallest enzyme concentration that gave a reasonable signal-to-noise ratio in our experiments was 0.2 mM, which is 20 times higher than the typical physiological concentration of the enzyme in cells. However, we believe that active substrate sensitivity could be improved after a proper optimization of SERS.

Conclusions. We found a distinct difference between the SERS spectra of Cu,Zn SOD1 and the zinc-deficient enzymes. Zinc-deficient SOD1 has a prominent Raman band at 1384cm^{-1} , which corresponds to the His-Cu mode, while the Raman band at 1295cm^{-1} due to Zn-His-Cu is absent. In contrast, the 1384-cm^{-1} Raman band was not enhanced in the case of Cu,Zn SOD1, while the 1295-cm^{-1} Raman band due to Zn-His-Cu can be clearly resolved. The smallest enzyme concentrations that gave a reasonable S/N ratio in our experiments was 0.2 mM. We believe that the sensitivity of the SERS can be im-

proved under proper optimization of SERS-active substrates, allowing noninvasive Raman *in situ* enzyme detection, as well as providing a way to monitor the effects of any treatment aimed at decreasing the levels of zinc-deficient enzymes within neurons.

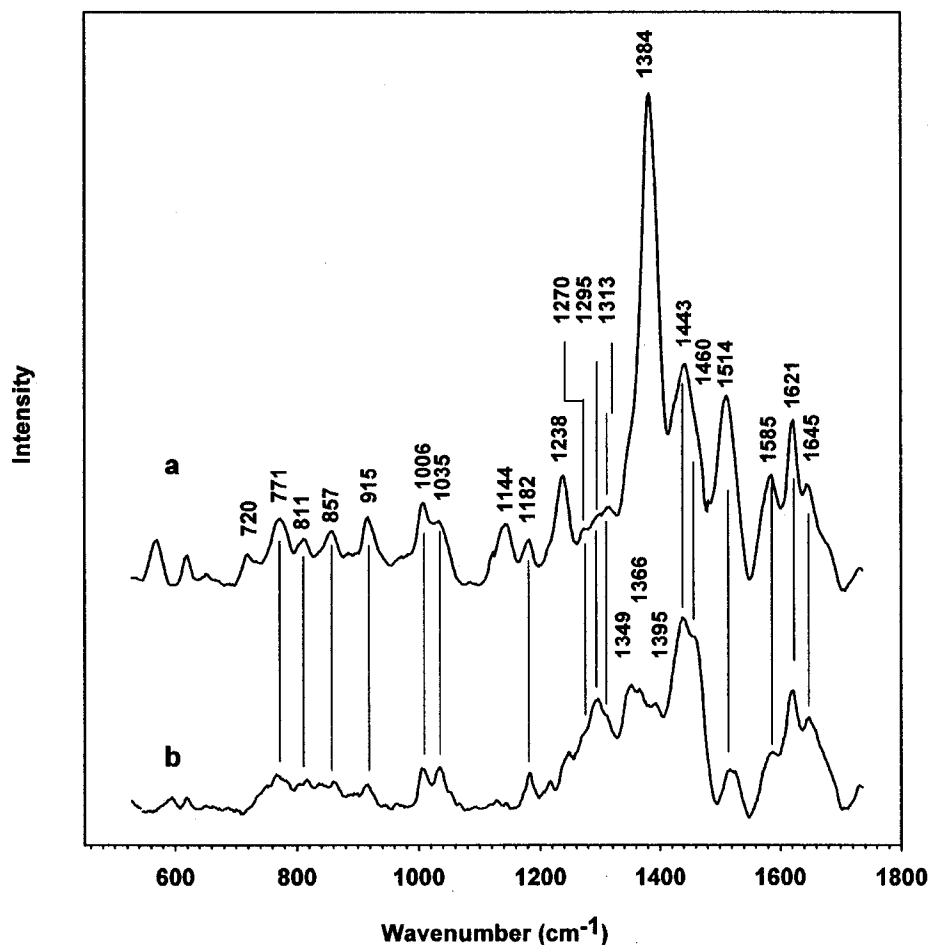


FIG. 31 SERS spectra of (a) zinc-deficient SOD1 and (b) Cu,Zn SOD1. The enzymes concentration was 0.4 mM. Spectra are an average of 500 acquisitions of one s each. The average laser power was 15 mW.

Study of SOD and hemoglobin by evanescent wave cavity ring-down spectroscopy.

Introduction

Cavity ring-down spectroscopy has proven to be an important technique for detection of small numbers of molecules in the gas phase. CRDS has recently been extended to liquid samples. The evanescent wave (EW) formed during internal reflection may interact with molecules present in the medium. CRDS is used to detect a very small change in absorption allowing a significant increase in sensitivity compared to other methods. The incorporation of dove prism with a ring-down cavity allows a simple implementation of EW-CRDS. This technique is particularly powerful if molecules have an affinity to the silica surface. In this manuscript, we present an application of EW-CRDS to study the interaction of charged proteins (hemoglobin and SOD) with a silica-water interface structure.

Material and methods

The experimental setup is shown in Figs. 32 and 33. We have used the doubled radiation of a LiF:F_2^{+++} CCC tunable laser specially designed for these experiments. The laser scheme is depicted in Fig. 32. The radiation of a Alexandrite laser at 730 nm has been used for the optical pumping of the LiF:F_2^{+++} crystal. CCC was placed in a "Z" type resonator in order to separate the pumping radiation of the Alexandrite laser and the oscillations of the CC laser. The first order of the diffraction grating (1200 g/mm, 700 nm blazed) was used to provide a positive feedback, while the zero order was used as an output. The oscillation frequency of the CC laser was doubled with a nonlinear BBO crystal. The laser radiation was directed into a 1-m-long cavity formed by two spherical mirrors,

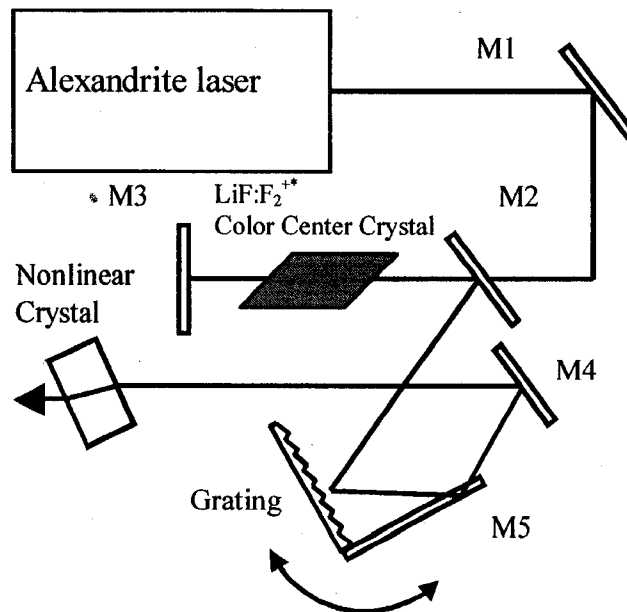


FIG. 32 LiF:F_2^{++} tunable color center laser.

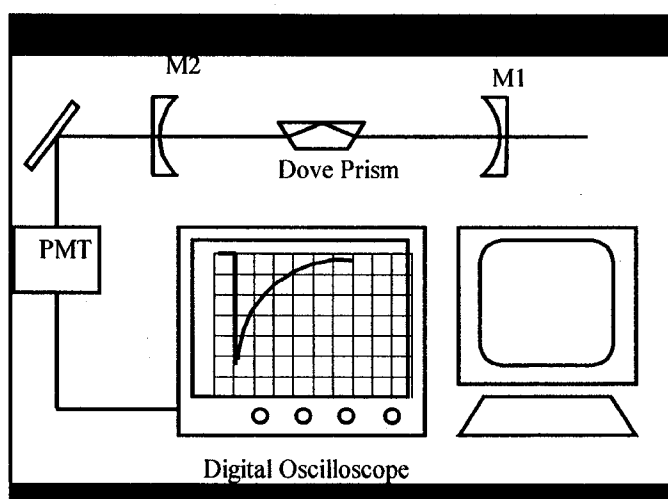


FIG. 33 Experimental setup for the EW-CRDS measurements.

with 99.96% reflection at 420 nm. The laser radiation was collimated in order to match the size of the cavity TEM_{00} mode. The dove prism was placed in the middle of the cav-

ity. The sample was carefully injected on the top of the prism, providing a necessary layer for the effective interaction of the evanescent wave with the absorbing molecules. The photon lifetime inside the cavity was monitored by a gated photo-multiplier tube (Hamamatsu, H7680). The data were collected and treated by the software based on LabView especially designed and written in our lab.

Results

Hemoglobin. The feasibility of the method was tested using hemoglobin molecules. The dynamic range of sensitivity of this method is shown in Figs. 34 and 35. The six curves correspond to different times of adsorption: a) 0, b) 5, c) 10, d) 15, e) 25, f) 30 min, respectively. The sensitivity dynamic range starts at a 0.1-mg/ml concentration of hemoglobin and goes up to 100 mg/ml. The shapes of the curves suggest that hemo-

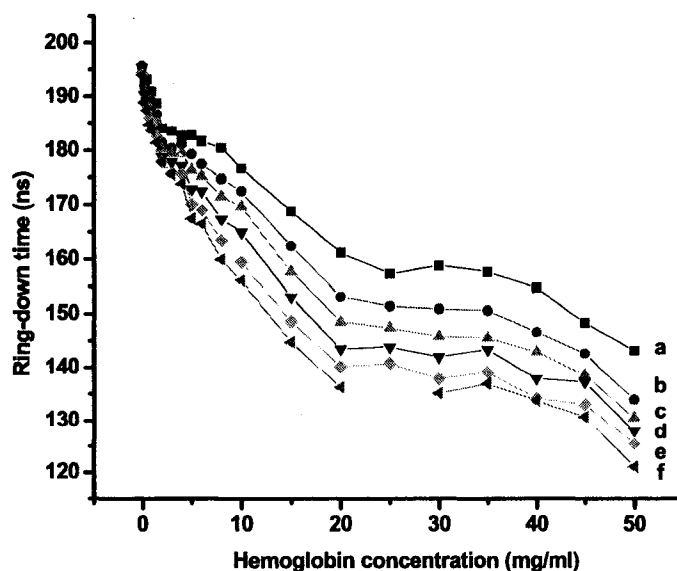


FIG. 34 Ring-time dependence on concentrations of hemoglobin at different adsorption times: a) 0 min, b) 5 min, c) 10 min, d) 20 min, e) 25 min, f) 30 min.

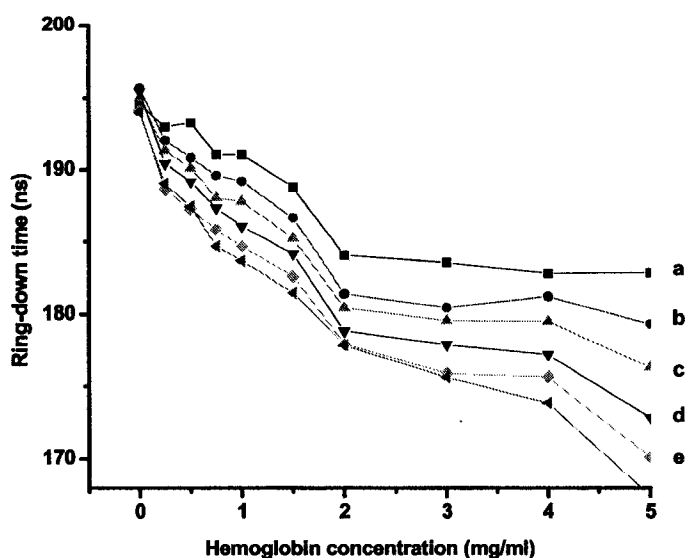


FIG. 35 Same as in Fig. 34 with zoomed low concentration region for the convenience.

globin forms layers on the silica surface. Two very distinctive layers can be seen between 2 mg/ml and 5 mg/ml, and 20 mg/ml and 40 mg/ml. The formation of the layer prevents additional adsorption of other molecules at a certain concentration. Therefore, one can observe saturation-like behavior of the ring-down time. If the concentration of analyte exceeds the threshold level, the new layer starts building up on top of the old one. Similar behavior was observed for several other molecules, such as organic dyes.

SOD. We tuned the radiation of a CC laser to 450 nm in order to better match the absorption wavelength of BCDA-Cu¹⁺ complexes. The dependence of ring-down time versus complexes concentration is shown in Fig. 36. As one can see, the sensitivity of CRDS is not ideal for this kind of analyte. Even for 10-fold concentration changes, the ring-down time changes only by 3%. Similar dependence has been observed for the

BCDA-SOD1 complexes. The possible explanation of poor sensitivity is the fact that BCDA-SOD1 has a weak affinity to silica surface.

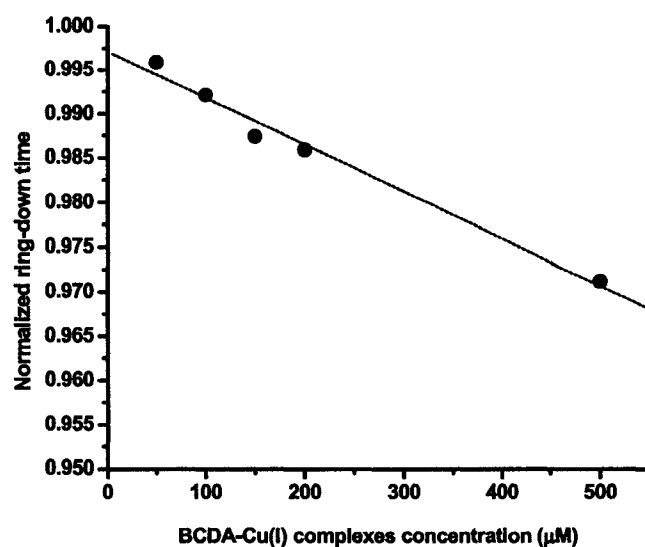


FIG. 36. Dependence of ring-down time from concentration of BCDA-Cu¹⁺ complexes after 15 minutes of adsorption.

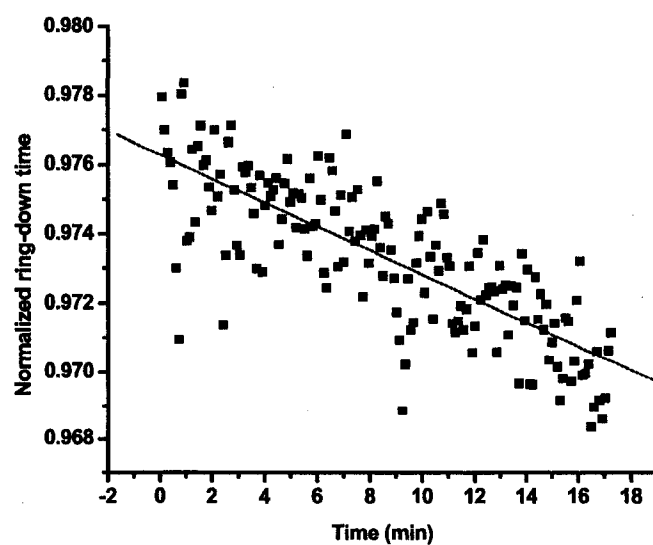


FIG. 37 Kinetics of BCDA-Cu¹⁺ complexes adsorption on the prism surface. The concentration of complexes was 500 μM.

Figure 37 shows the kinetic of complexes adsorption for the highest concentration used in our experiment (500 μM). As one can see, the ring-down time changed only slightly (about 0.7%), clearly indicating a weak interaction of BCDA-SOD1 complexes with a prism surface.

Nevertheless, if one were to modify the surface in such a way that the BCDA-SOD1 complexes had a high affinity to it, we expect that SRDS would provide sufficient sensitivity to study the physiological level of BCDA-SOD1 complexes *in vitro*.

Raman study of degree conversion (DC) and PC of dental restorative materials.

Introduction

Dental practitioners are demanding better restorative materials. The search for such materials, exhibiting the appropriate physical and mechanical properties, has resulted in the introduction of light-cured polymer composites. The major components of light-cured composites are BIS-GMA, TEGDMA, camphorquinone, and silane-treated microparticles (80%).

These composites have a major drawback, in that the degree of cure is proportional to the amount of light and light wavelength to which they exposed. So composites polymerized to a certain depth, called depth of polymerization (DP), and cure to a certain degree or DC. Because dental restoration needs an optimal polymerization level, investigators have studied the effect of different parameters, such as the intensity and wavelength of curing light, on the depth of polymerization and DC.

The usual methods are microhardness measurements, scraping tests, and IR spectroscopy. MicroRaman has an obvious advantage when compared to other methods due

to the high spatial resolution (about 1-10 μm). The goal of this study is to evaluate the depth of polymerization and DC at various wavelengths of curing light using Raman spectroscopy.

Materials and methods

We have used two light-cured composites, Esthet X, Shade A2, and Spectrum TPH, Shade A2, obtained from Dentsply. The composites were injected into a brass mold with a dove-happed inlet 5 mm wide and with a 6-mm dip. The mold and composites were heated to 38 degrees prior to injection and kept at the same temperature during irradiation.

The experimental setup for composites curing is shown in Fig. 38. The emission of 500-W Hg lamp (Oriol) at 365 nm, 404 nm, 435 nm, 565 nm have been used for curing. The radiation of 488-nm Argon-ion laser and a QTH curing lamp (Spectrum 800, Dentsply) have been used for curing as well. The radiation of the Hg lamp was directed to the 1/8-m focal length monochromator (Oriol 7240) equipped with a 1200-g/mm grating blazed to 500 nm. The slits of the monochromator were completely opened (5 mm) to maximize the output power. The spectral window width of the monochromator output was about 20 nm. A two-lens collimator was used to provide the beam divergence equivalent to the divergence of the Spectrum 800 (Dentsply) curing light. The power of curing radiation at different wavelengths was measured with a power meter (Power Max 5200, Molectron). The final irradiation dosage (power density times irradiation time) was adjusted to be equal to 16 J/cm^2 ; i.e., equivalent to the irradiation of a sample by a curing light with power density 400 mW/cm^2 during 40 s ($400 \text{ mW} \cdot 40 \text{ s/cm}^2 = 16 \text{ J/cm}^2$). The

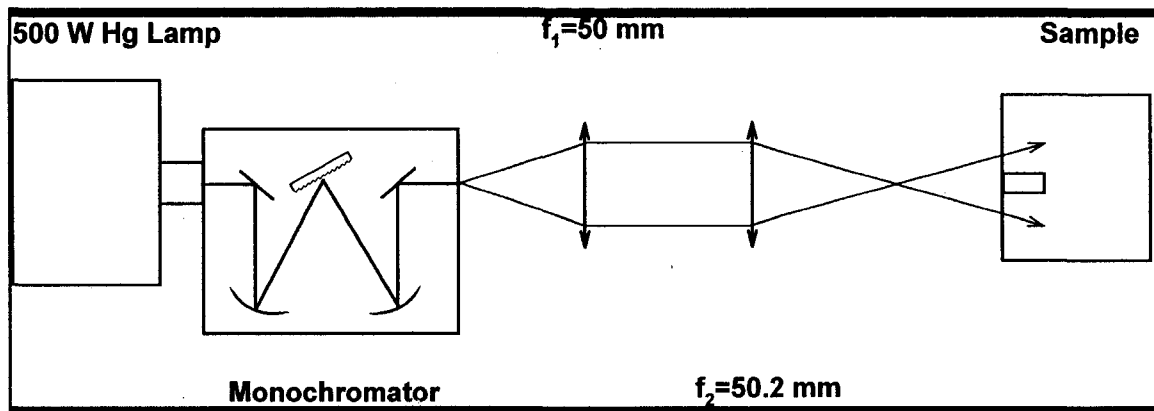


Fig .38 Experimental setup used for composites curing by a different wavelength.

TABLE 1. The output power density at different wavelengths and corresponding irradiation times.

Wavelength	Power density (W/cm ²)	Irradiation time (s)
366 nm	104	153
404 nm	88	181
435 nm	198	80
488 nm	80	200
565 nm	240	67

The output power density at different wavelength and corresponding irradiation times needed in order to obtain 16J/cm², which is equivalent to irradiation of sample by a curing light with power density 400mW/cm² during 40s (400mW*40s/cm²=16J/cm²).

output power density at different wavelengths and corresponding irradiation times is shown in Table 1.

The composites absorption (attenuation) spectra were taken by a Shimadzu spec-

trophotometer. The composites were compressed between microscope slides making layers about 100- μm thick. Two microscope slides with a thin composites layer in-between were then placed in spectrophotometer mount.

The Raman spectra of cured samples were taken at different locations from the curing site using the Dilor XY MicroRaman imaging system equipped with an LNC CCD camera. The MicroRaman system was operated in single grating mode with a super-notch filter installed for the rejection of excitation radiation. The radiation of Argon-ion laser at 642 nm was used for excitation. The power of laser radiation at the sample's surface was about 100 mW. The use of the microscope objective (Olympus x 10) allowed the collection of spectra from the area about 80 μm^2 large. All Raman spectra are an average of 100 acquisitions of 1 s each.

The DC was determined by comparing the intensity of the vibration band at 1640 cm^{-1} of the C=C double bond of the vinyl group and the aromatic C=C stretching band at 1610 cm^{-1} . The intensity of the band at 1610 cm^{-1} was used as a standard, since the concentration of aromatic groups does not change due to polymerization.

The DC was calculated as follows:

$$DC(\%) = \left(1 - \frac{R_{pol}}{R_{unpol}} \right) \times 100\% , \quad (5)$$

Where $R_{pol} = \frac{I_{1640}^{pol}}{I_{1611}^{pol}}$ is a ratio of intensities of 1640 cm^{-1} and 1611 cm^{-1} bands of

polymerized samples, and $R_{unpol} = \frac{I_{1640}^{unpol}}{I_{1611}^{unpol}}$ is a ratio of intensities of 1640 cm^{-1} and 1611 cm^{-1} bands of unpolymerized samples.

However, due to the relatively low signal-to-noise ratio of the obtained spectra,

simple comparison of Raman bands intensities would lead to large error values. Therefore, we fitted experimental data by using the Gaussian deconvolution method. The following protocol of the data correction has been used. At first, we combined all spectra in the same group of samples (for example, uncured Esthet X) in order to have a better signal-to-noise ration. Deconvolution of the combined spectrum revealed three Raman bands at 1611 cm^{-1} , 1640 cm^{-1} , and 1718 cm^{-1} , corresponding to aromatic C=C stretching, C=C double bond vibration of the vinyl group, C=O bond vibration, and a broad background. Next, the parameters that are responsible for band position and FWHM were fixed, and all spectra were fitted by intensity only. The results of this procedure are shown in Fig. 39. Finally, background was subtracted and intensities of Raman bands revealed and compared. Two corrected spectra of uncured and cured Esthet X composite are depicted in Fig. 40 for comparison.

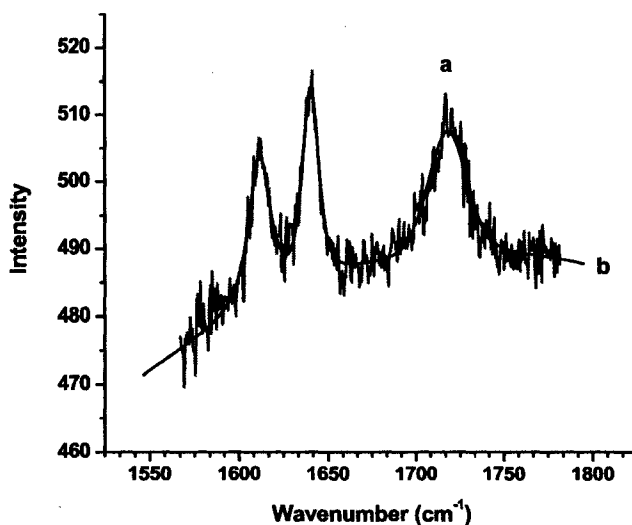


FIG. 39 Reconstruction of Raman spectrum of uncured Esthet X composite with a Gaussian deconvolution method: a) untreated Raman spectrum and b) reconstructed Raman spectrum. Raman bands at 1611 cm^{-1} , 1640 cm^{-1} , and 1718 cm^{-1} corresponding to aromatic C=C stretching, C=C double bond vibration of vinyl group, and C=O bond vibration.

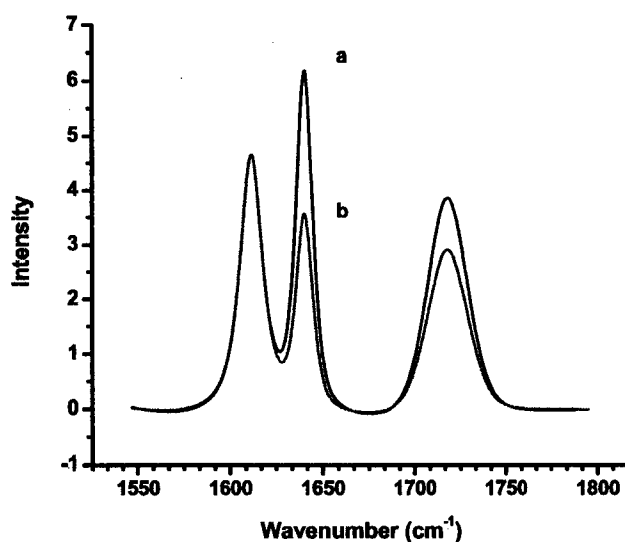


FIG. 40 Reconstructed Raman spectra of a) uncured Esthet X composite and b) Esthet X composite cured by QTH lamp. The background was subtracted. Raman bands at 1611 cm^{-1} , 1640 cm^{-1} , and 1718 cm^{-1} corresponding to aromatic C=C stretching, C=C double bond vibration of vinyl group, and C=O bond vibration.

Results

The results of the Raman study show a good correlation with the other methods used. The DC as well as PC showed a strong dependence on the wavelength of the curing light. These dependences are shown in Figs. 41 and 42 for Esthet X and TPH composites, respectively. There was no sample polymerization observed in the case of a 565-nm wavelength of curing light. These points are thus not shown in Figs. 41 and 42. The DC for the shorter wavelength was better or the same when compared to quartz-tungsten-halogen (QTH) or Argon-ion laser cured samples. However, the PC was smaller for the shorter wavelengths. There are two possible reasons for that phenomenon. The attenuation of light is greater for the shorter wavelengths, as in Fig. 43. The second possible reason is that the absorption of camphorquinone has a maximum at approximately 472

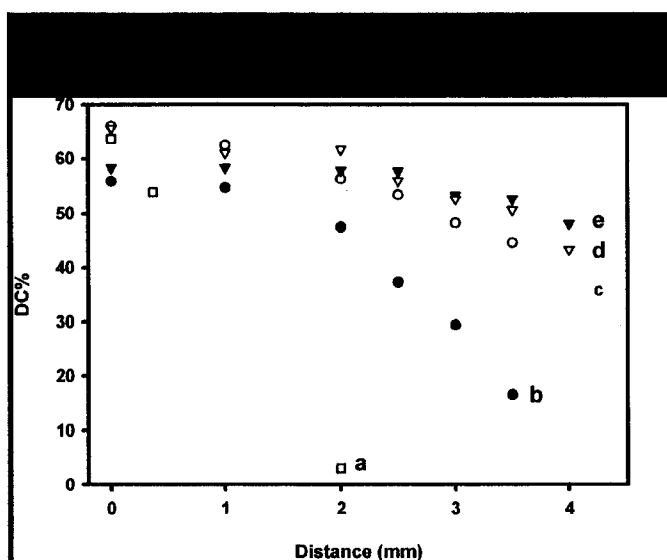


FIG. 41 Degree of conversion (DC) of Esthet X, Shade A2 composite for the different wavelengths of curing light: a) 366 nm, b) 404 nm, c) 435 nm, d) QTH curing lamp (Spectrum 800, Dentsply), and e) 488 nm radiation of Argon-ion laser. The irradiation dose was equal to 16J/cm² for all samples and was adjusted by varying irradiation time; that is equivalent to irradiation of sample by a curing light with power density 400 mW/cm² during 40 s (400 mW*40 s/cm²=16 J/cm²).

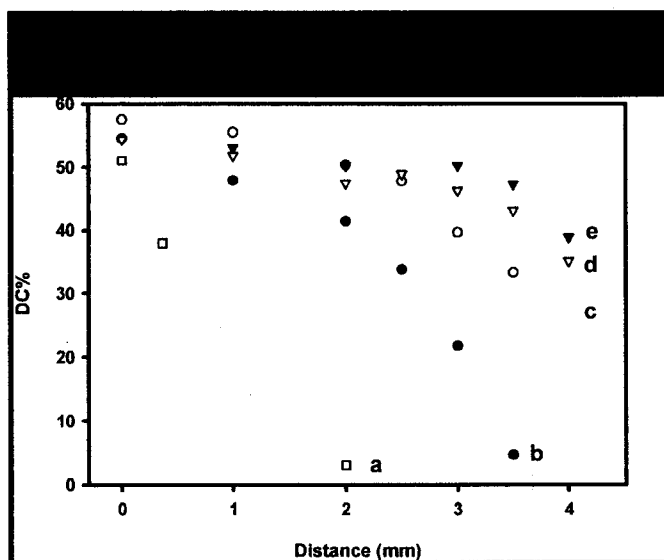


FIG. 42 DC of TPH, Shade A2 composite for the different wavelengths of curing light: a) 366 nm, b) 404 nm, c) 435 nm, d) QTH curing lamp (Spectrum 800, Dentsply), e) 488-nm radiation of Argon-ion laser. The irradiation dose was equal to 16 J/cm² for all samples and was adjusted by varying irradiation time, that is equivalent to the irradiation of sample by a curing light with power density 400 mW/cm² during 40 s (400 mW*40 s/cm²=16 J/cm²).

nm with a FWHM about 70 nm. Thus, the wavelengths shorter than 440 nm require a higher power density for the adequate initiation of a polymerization reaction.

The highest curing depth was observed for the monochromatic radiation of an Argon-ion laser at 488 nm for both composites. It was even better than for the QTH lamp,

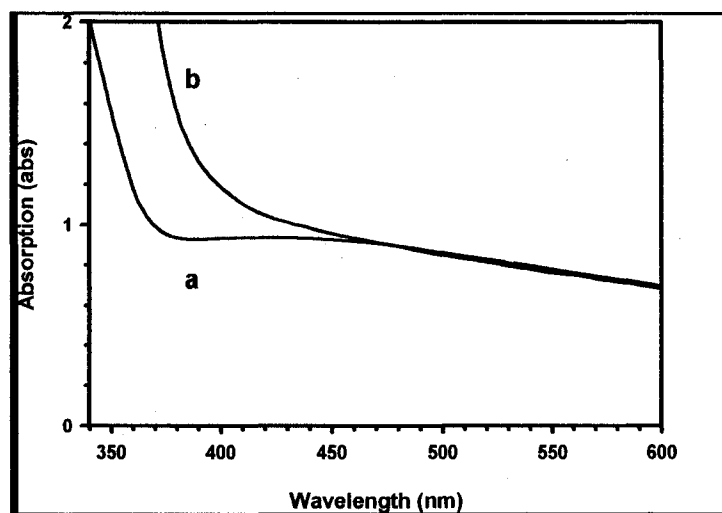


FIG. 43 The absorption (attenuation) spectra of (a) TPH, shade A2 composite material and (b) Esthet X, shade A2 composite material. Spectra were normalized at 480 nm for convenience.

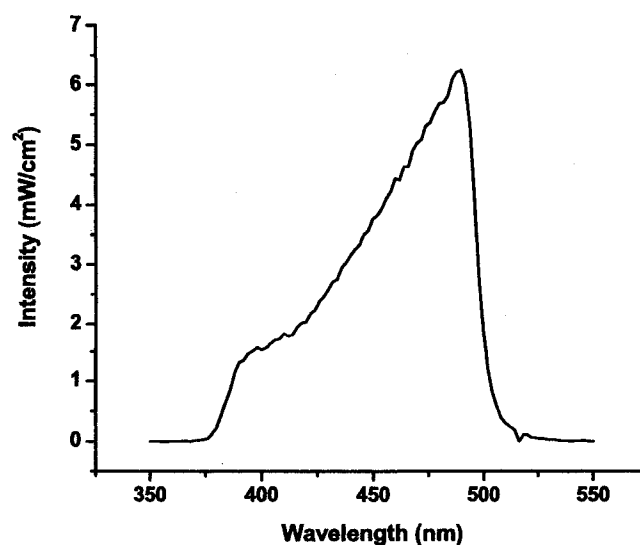


FIG. 44 Emission spectrum of Spectrum 800 (Dentsply) curing light.

which has a wide emission spectrum (Fig. 44). The DC for the 488 nm was more homogeneous and decreases slowly in depth of sample. However, the DC at the curing site was less than for the QTH lamp or shorter wavelengths. This difference is seen especially in the case of the Esthet X composite, where the difference in DC was about 7 %. Remarkably, the highest value of DC at the curing site was in the case of the 435-nm curing wavelength for the both composites. It was 66 % and 58 % for Esthet X and TPH respectively.

The results of our study also show that the power density of curing light is not the most crucial factor for the polymerization. As one can see, the DC and PC of the composites were comparable with samples cured with the QTH lamp. However, the power densities given in Table 1 were less than 400 mW/cm^2 ; in fact, it was only 80 mW/cm^2 for the 488-nm curing wavelength.

Conclusions

The ideal curing lamp should have two narrow emission bands around 435 nm and 480 nm. The band at 435 nm will give the highest value of DC on the curing site, while the 480 nm band will provide the best curing depth.

Laser breakdown spectrometer for environmental monitoring

Introduction

Laser-induced breakdown spectroscopy (LIBS) is a rapid, real-time analytical method. It is based on the spectral analysis of the plasma generated by laser pulses. The power densities can exceed hundreds of MW/cm^2 if laser radiation is focused into a small

spot on a sample material. A laser spark or microplasma occurs at such a high radiation power with a high temperature and electron density. The initial temperature could be as high as 10^7 °C. At such a high temperature, any sample material is decomposed, vaporized, and ionized. The energy is released over a broad range of the spectrum, from soft X-rays to the near IR, at the early stages of plasma. This emission can be effectively gated by the detection system. As the plasma plume evolves, the plasma cools down and neutral atoms in excited states are formed. The spectral analysis of the atomic emissions yields a fingerprint of the atomic species presented in the sample.

The characteristics of LIBS can be found in review papers [54-68]. The variety of applications such as alloy and metal surface analysis [59,60], gas [61], liquid [62,63,74] and environmental sample analysis [75,77] have been reported.

Simultaneous multi-element analysis in real time is the greatest advantage of LIBS. No sample preparation is needed. The procedure could be fully automated and therefore does not require extensive operator training. Application of optical fiber makes possible the construction of a simple and compact device for real-time remote sensing of solid, liquid, and gaseous samples.

Cremers *et al.* [64] demonstrated direct LIBS detection of atomic species in water with detection limits on the order of several ppm for a number of atomic elements. Arca *et al.* [65] demonstrated the feasibility of quantitative determinations of trace elements in water by LIBS. However, the described experimental setup utilized high-energy (400 mJ) laser pulses focused on the free surface of the water sample. To avoid possible interference from bubbles formed by preceding sparks, the system required a relatively low repetition rate (1 Hz) and relatively long averaging acquisition time. Nakamura *et al.* [66] reported LIBS detection of Fe concentrations of less than 20 ppb using sequential laser

pulses of two high rep rate (20 Hz), Q-switched Nd:YAG lasers and a continuous flow of water-purge gas aerosol.

The aim of this study was to demonstrate that by a proper optimization of experimental setup in terms of laser pulse, sample delivery characteristics, sampling geometry, and the time-, spatially-, and spectrally-resolved detection system, a real-time quantitative determination of trace element concentrations in water by LIBS becomes feasible. The motivation of this study was to construct a simple, field-operated LIBS instrument for fast *in situ* analysis of heavy metals with a wide dynamic range of detection and sensitivity adequate for trace pollutant monitoring.

First, some of the specific problems will be discussed and the optimization of the experimental setup will be described. Some results of actual analyses then will be reported, and suggestions for further improvements that will be presented.

Experimental Arrangements

The overall system design is shown in Fig. 45. The LIBS system consists of four principal components: laser breakdown atomizing module; collection optics; spectrally selective time-resolved detection, and data acquisition system.

The atomizing module serves as a reservoir of excited atoms. It includes a pulsed laser source and a system for sample delivery to the laser spark. Fluorescence of excited atoms is effectively collected and focused into the entrance slit of spectrograph. The fluorescence signal is spectrally selected and acquired by a gated, intensified CCD camera.

A computer controls the spectrograph and CCD camera. The same computer is used to collect and analyze the experimental data. We developed virtual instrument driv-

ers based on the LabView[®] software for the Windows platform for flexibility in data acquisition and instrument control. A calibration curve for a particular instrument can be constructed from measurements of the amplitude or peak areas of the fluorescence lines for different concentrations in a series of etalon samples.

The described experimental setup is based on a 0.75-m spectrometer ARC-750 (Acton Research Corp.); intensified TE-cooled 256 x 1024 CCD camera (Princeton Instruments); a probe with fiber optic guide for signal transportation; and an atomizer based on Nd:YAG laser (50-100 mJ at 1.064 μ m, 7-ns pulse duration at a 10-Hz repetition rate, with injection seeding for temporally and spatially stable output pulse operation) generating plasma in the water jet of a continuously circulating sample.

We used two different methods of sample delivery for atomization in plasma plume. In the first one (Fig. 45), the liquid solution is delivered into the chamber of the nebulizer, where argon-gas-assisted aerosol is formed and delivered via nozzle to the plasma plume generated by a laser pulse.

The second approach (Fig. 46) is based on the direct generation of plasma in the water jet of a continuously circulating sample. The impurities are atomized and ionized and emit fluorescence in a plasma plume. Fluorescence light was collected by an elliptical mirror, directed through the fiber bundle to the slit of the spectrograph, and subsequently measured in real time with the multichannel detection system.

It is important to optimize the collection system, since the attainable signal is proportional to the fluorescence collection efficiency. Our collection system uses an elliptical mirror, where the laser spark is generated near one of the focal points. The multifiber bundle was placed into the second focal point, transmitting the collected fluorescence to the entrance slit of the spectrograph. The exit end of the fiber bundle is

arranged to have a rectangular shape (4 x 0.1 mm) to match the entrance slit. A TE-cooled 256 x 1024 CCD camera (Princeton Instruments) with a fiber-coupled intensifier was used for time-gated detection of fluorescence signals under pulsed laser excitation. The intensifier is “closed” under normal conditions, and no photoelectrons reach the CCD detector. The pulse generator PG-200 (Princeton Instruments) produces a short, high-voltage (200-V) pulse to gate the detector for a 10-500 μs exposure, 1-15 μs after a nanosecond laser pulse, allowing the continuum emission to decay. A single grating monochromator ARC-750 (Acton Research Corp.) with aperture ratio $f/10$ and focal length 750 mm was operated as a spectrograph. The multichannel CCD detector was mounted at one of the output ports of the spectrometer. The spectral resolution of this system was estimated to be less than 0.04 nm at 633 nm for a 1200 g/mm grating measured with input slit width of 10 μm . In our experiments, we used 2400 and 1200 g/mm gratings for UV and UV-VIS measurements, respectively.

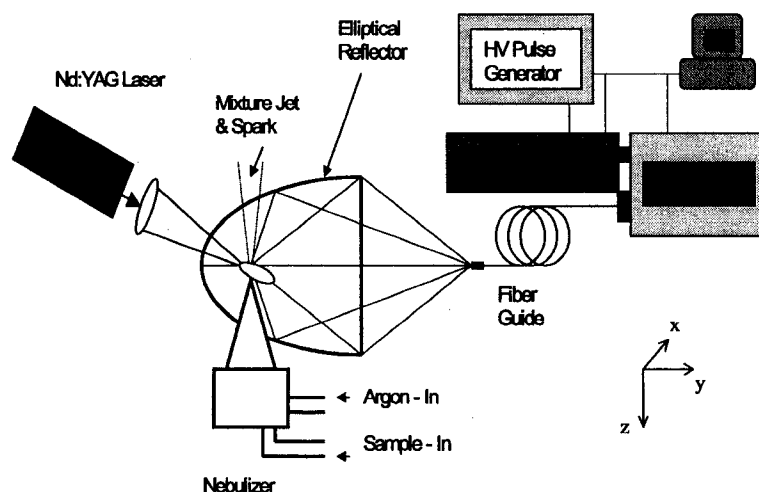


FIG. 45. LIBS System Design with argon-water aerosol sample delivery.

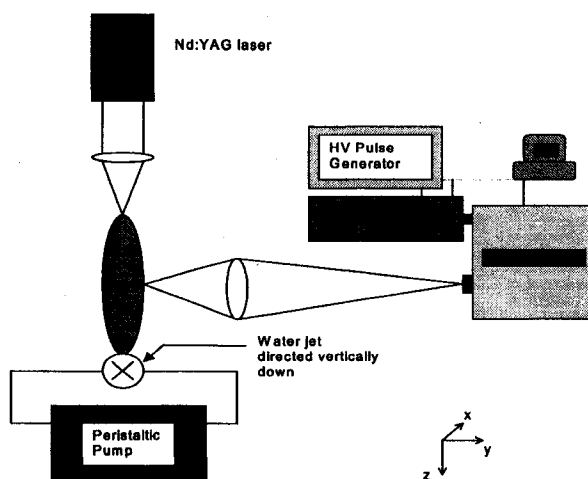


FIG. 46. LIBS System Design with direct generating plasma in the water jet of a continuously circulating sample.

We performed a series of measurements on various reference water samples, with the goal of finding an optimum time delay from the laser pulse and the beginning of the LIBS spectra acquisition, as well as optimum gate duration.

Time evolution of the LIBS spectra of Cu (500 ppb)-contaminated water generated by the Nd:YAG laser radiation (1064 nm, 60 mJ) and measured at 1, 7, 15, and 25 μs after the laser pulse is shown in Fig. 47. The earlier stages of plasma discharge (gate delay $< 1 \mu\text{s}$) are characterized by continuum emission demonstrated in Fig. 47. The subsequent temporal stages of the plasma have a “fingerprint” emission pattern of Cu atoms at 324.76 and 327.4 nm.

Recently, Lee et. al [57] showed that the selection of the analytical location in the plasma is crucial for achieving the highest signal-to-background noise ratio of analytical atomic lines and to avoid self-absorption and line broadening. The spatially resolved LIBS spectra of the Cu (10 ppm)-contaminated water sample generated by the Nd:YAG

laser is demonstrated in Fig. 48. The spectra were measured at distances of 5, 3, 2, 1, 0, and -1 mm from the continuously flowing water jet. The spectra were detected using the adjustable features of the atomizer [see Fig. 45 (b)]. Two XYZ positioning mounts provided simultaneous and/or independent XYZ motion of the water jet and the laser radiation focusing lens with respect to the fiber bundle or the input slit of the spectrograph.

The highest signal-to-background noise ratio corresponds to the plasma slice located 2 mm in front of the water stream as seen in Fig. 48. The same procedure has been repeated for different elements. We did not find any noticeable differences in spatial behavior of the optimal plasma locations.

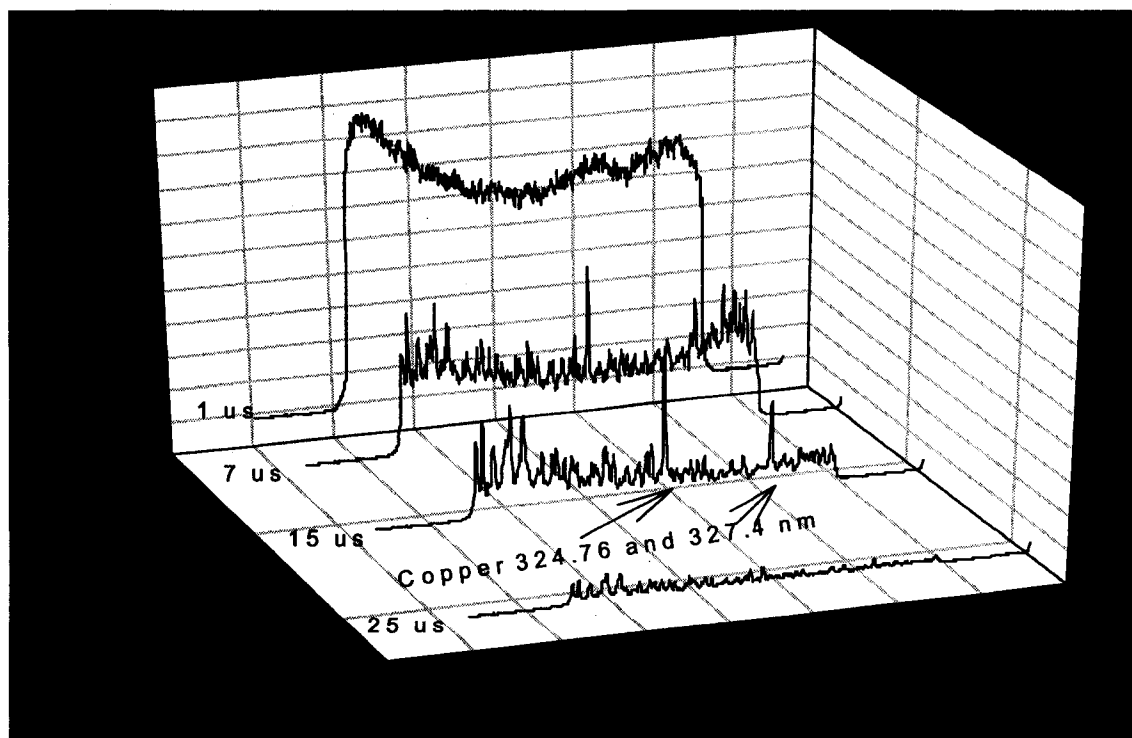


FIG. 47. Time evolution of the LIBS spectrum for water containing 500 ppb Cu. Plasma is generated by Nd:YAG laser 1064 nm radiation in the water jet of continuously circulating sample. The spectra were obtained by averaging 30 acquisitions with gate duration of 10 μ s.



FIG. 48. Spatially resolved LIBS spectrum of Cu (10-ppm) contaminated water sample generated by the Nd:YAG laser and measured at distances 5, 3, 2, 1, 0, and -1 mm from the continuously flowing water jet.

Water-argon gas aerosol LIBS measurements

Samples containing different concentrations of Al, Cd, Cu, Fe, Pb, and Zn ions were tested. The reference samples were measured with a Thermal Jarrell Ash Atom-SPEC GF Workstation atomic absorption spectrophotometer (AAS).

The heavy metal ions concentrations in LIBS measurements were determined by comparing intensities of the characteristic lines of a given element to the corresponding intensities measured on the reference sample. The actual concentrations of the heavy metals in samples were also determined with the graphite furnace AAS.

The results of our measurements are summarized below. Unless otherwise stated, the Nd:YAG laser was operated at an average power of 10 Hz, with 100 mJ energy per pulse. The resulting detection limits ranged from 2 ppm to 30 ppm. This is within the range of the TABLASER system delectability [77]. Sdorra and Niemax detected Mg samples as well as Zn samples at approximately the same wavelengths and intensities [78]. The results for each sample were graphed (concentration vs. relative intensity) to

verify the validity of the experiment. Each element had a linear graph similar to that of Quentmeier, Sdorra, and Niemax [78].

Aluminum (Al). For aluminum, the fluorescence signals at 394.4006 nm and 396.1520 nm were used (see Fig. 49). This emission transition was $^2S_{1/2} (3s^24s) \rightarrow ^2P^0_{1/2} (3s^23p)$ for 394.4006nm. The emission transition for 396.1520 nm was $^2S_{1/2} (3s^24s) \rightarrow ^2P^0_{3/2} (3s^23p)$. The gate delay and width were optimized for best results to 15 μ s and 500 μ s, respectively. With the single laser-system, the detection limit of aluminum was approximately 30 ppm.

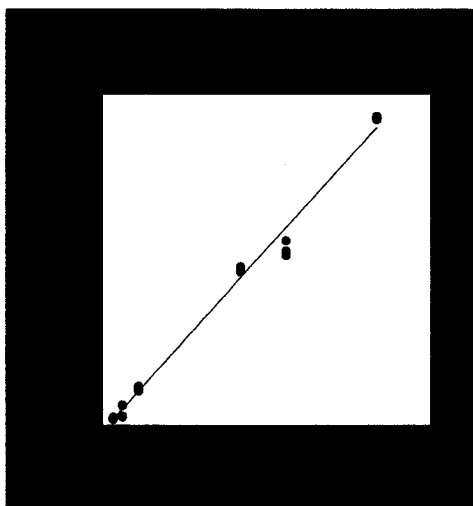


FIG. 49. LIBS signal corresponding to Al line 394.4006 nm vs. LIBS-determined concentration (mg/L)

Cadmium (Cd). The optimum gate delay and width for cadmium were 2 μ s and 250 μ s, respectively (Fig. 50). The fluorescence signal at 228.8022 nm was used. The limits of detection for cadmium in this system were approximately 30 ppm.

Copper (Cu). The copper fluorescence signals were detected at 327.3957 nm as well as at 324.754 nm (Fig. 51). The gate delay was optimized at 15 μ s and the gate width at 35 μ s. Copper had a detection limit of 3.25 ppm. The emission transition of copper detected at 324.754 nm was $^2P^0_{3/2}(3d^{10}4p) \rightarrow ^2S_{1/2}(3d^{10}4s)$. The emission transition detected at 327.3957 nm was $^2P^0_{1/2}(3d^{10}4p) \rightarrow ^2S_{1/2}(3d^{10}4s)$.

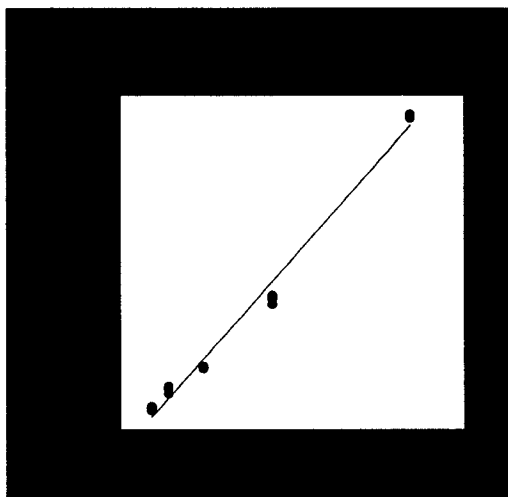


FIG. 50. LIBS signal corresponding to Cd line at 228.8022 nm vs. LIBS-determined concentration (mg/L)

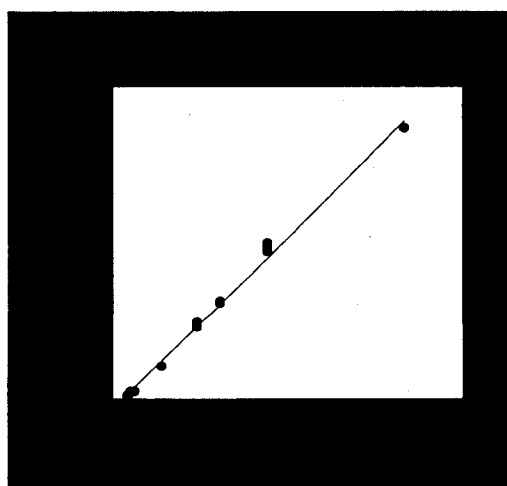


FIG. 51. LIBS signal corresponding to Cu line at 324.754 nm vs. LIBS-determined concentration (mg/L).

Iron (Fe). Iron had an optimized gate delay and gate width of 24 μs and 30 μs , respectively. Iron was detected at four wavelengths (Fig. 52). Those wavelengths were 248.32718, 250.1132, 252.28505, and 256.6901 nm. Iron had a detection limit of approximately 30 ppm. The emission detected at 248.32718 nm was ${}^5\text{F}_5^0 \rightarrow {}^5\text{aD}_4$ ($3\text{d}^64\text{s}^2$). The emission detected at 250.1132 nm was ${}^7\text{P}_3^0 \rightarrow {}^5\text{aD}_4$ ($3\text{d}^64\text{s}^2$). The transition at 252.28505 nm was found to be ${}^5\text{xD}_3^0 \rightarrow {}^5\text{aD}_4$ ($3\text{d}^64\text{s}^2$). The last transition at 256.6901 was found to be ${}^5\text{xD}_4^0 \rightarrow {}^5\text{aD}_4$ ($3\text{d}^64\text{s}^2$).

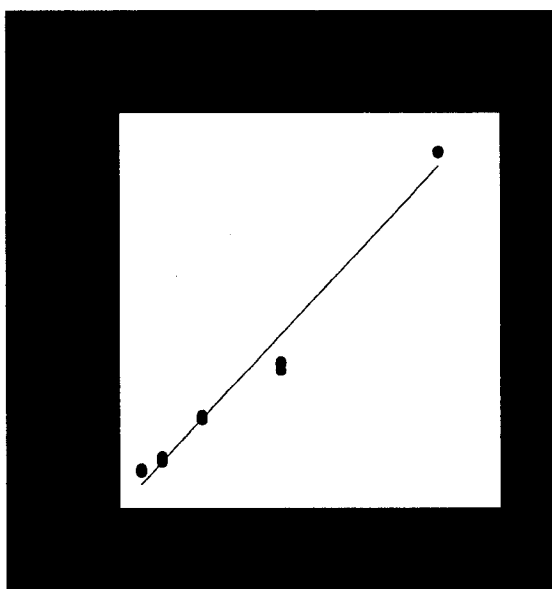


FIG. 52. LIBS signal corresponding to Fe line at 248.327 nm vs. LIBS-determined concentration (mg/L).

Lead (Pb). Lead was detected at 405.7807 nm, with a gate delay of 25 μs and a gate width of 50 μs . Once again, the delay and width were optimized to fit the element under investigation. Lead's limit of detection was found to be about 30 ppm (Fig. 53). The transition of lead was shown to be ${}^3\text{P}_1^0$ ($6\text{p}7\text{s}$) \rightarrow ${}^3\text{P}_2$ (6p^2).

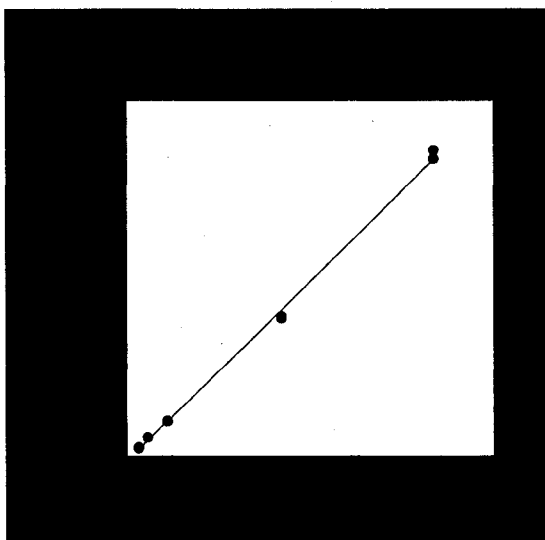


FIG. 53. LIBS signal corresponding to Pb line at 405.78 nm vs. LIBS-determined concentration (mg/L)

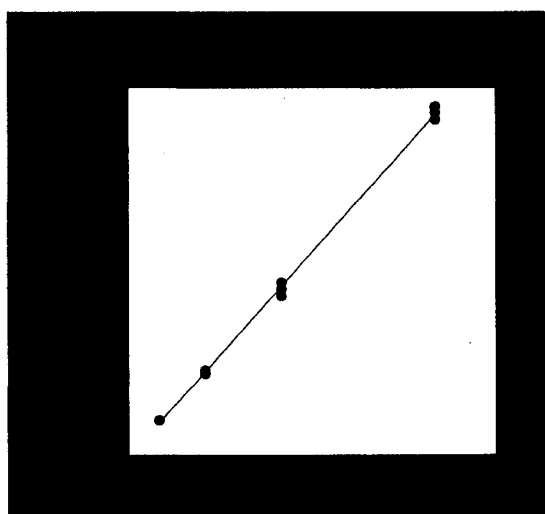


FIG. 54. LIBS signal corresponding to Zn line at 213.856 nm vs. LIBS-determined concentration (mg/L)

Zinc (Zn). Zinc had an optimized gate delay and width of 10 μ s and 1 μ s, respectively. Zinc was detected at 213.856 nm (Fig. 54). This element had a detection limit of 30 ppm. Both clean and contaminated matrix samples of zinc were examined. They had approximately the same spectra and the same detection limits. This is especially impor-

tant because it shows that the plasma generation system is not dependent on the sample's preparation.

Our measurements showed a good dynamic range with linear dependence of the LIBS signal vs. trace pollutant concentrations for samples containing Al, Cd, Cu, Fe, Pb, and Zn ions comparable to the results using atomic absorption spectrophotometry. Initial indications showed good agreement (within 10%) between these two methods. However, the resulting detection limits, ranging from 2 ppm to 30 ppm, were not satisfactory. Nevertheless, we expect further improvements by optimization of sample delivery characteristics, sampling geometry, detection timing, and spectrograph throughput.

The preliminary studies showed that heavy metal atomic emission in Ar plasma is significantly suppressed with respect to atomic line emission in air or He plasma. Therefore, the optimization of sample delivery characteristics and substitution of Ar purge gas with an open-air system could improve detection limits.

LIBS measurements when plasma is generated in the water jet of continuously circulating sample.

The known concentrations of Cu and Cr ions were tested by LIBS. The reference water samples were measured with an AAS with graphite furnace for quantitative analysis. The concentrations of the heavy metals were determined by comparing the LIBS intensity of the characteristic lines of a given element to the corresponding intensities measured using the reference samples. In addition, the samples were characterized with the AAS. The experimental results are shown in Fig. 55.

The linearity of the LIBS signal vs. trace pollutants was observed, as shown in Fig. 55. The experimental error for Cu concentration measurements was found to be

around 10%. The detection limits of 100 ppb for Cu and Cr atoms were achieved.

The primary drinking water goal for Cu (40 CFR D Subpart F 141.51) of 1.3 mg/L (ppm), and a secondary drinking water quality maximum contaminant limit of 1.0 mg/L were established by the U.S. Environmental Protection Agency. The EPA drinking water goal is 170 mg/L for Cr^{+3} and 50 $\mu\text{g/L}$ (ppb) for Cr^{+6} . The criteria for the protection of aquatic life is about 10 ppb of Cu, and about 200 $\mu\text{g/L}$ of Cr^{+6} , for typical hardness levels. Therefore, the achieved detection limits for these metals are quite suitable for evaluations of drinking water safety and for the protection of aquatic life. The LIBS results are therefore very important in view of applications for in-field continuous monitoring of water.

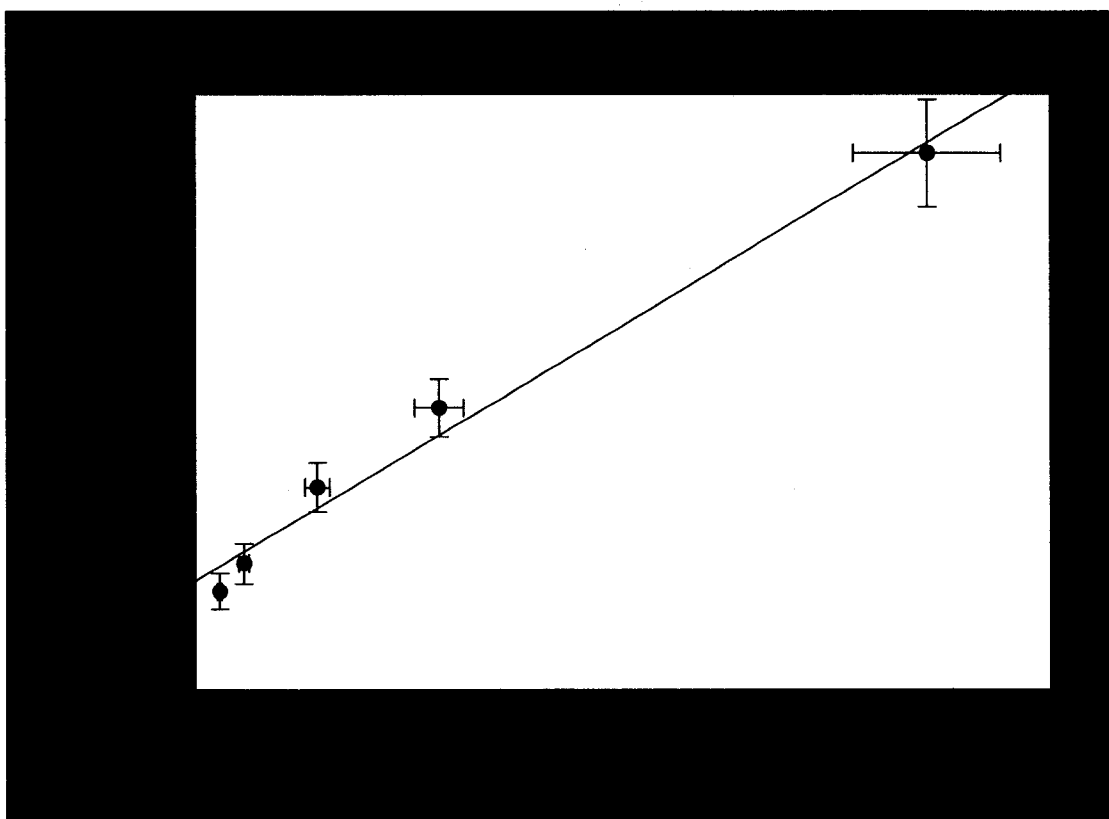


FIG. 55. LIBS signal for Cu polluted water vs. LIBS-determined concentration (ppb). The results correspond to Cu atomic line at 324.754 nm.

Conclusions

The results reported in this paper demonstrate the following: (1) LIBS is a feasible technique for real-time monitoring of trace element detection in water; (2) The method described here provides direct and continuous determinations of Cu and Cr in water as low as 100 ppb, less than or close to the EPA criteria for Cu and Cr in drinking water and for the protection of aquatic life; (3) The wide dynamic range of LIBS detection makes it very attractive for in-field monitoring of water quality with different levels of pollution without the need for special sample preparation; (4) Simple cell-less sample delivery results in easy handling; (5) and Continuously circulation or pumping of new sample water provides an opportunity for on-line measurements and suppresses interferences from bubbles formed by the preceding sparks.

The achieved detection limits promise a new application for LIBS in sensing biological warfare agents. It is proposed to tie the detection of bioagents (e.g., anthrax spores) to the detection of heavy metal atoms that can be selectively attached to the spores. The method is pretty straightforward and is completely analogous to fluorescent-labeled-antibodies biosensing. Antibodies are substituted by special ligands featuring a selective affinity to anthrax spores and, instead of dye labeling, one may use heavy metal microspheres. The size of the metal microsphere (4 μm) can be chosen to match the average size of the anthrax spores. On average, each spore can be bonded to one metal microsphere. Simple calculations show that each 4- μm metal microsphere contains about 10^{12} atoms of metal. A 100-ppb level of detectability of the method corresponds to $\sim 10^{15}$ atoms/cm³, or 1000 spores per 1 cm³ of water. For an ambient air intake volume of 10 m³ forced through 10 cm³ of water in the accumulation chamber, the final detectability of the proposed system turns out to be ~ 1000 spores/m³, which is lower than health dan-

ger levels. The metal detection limits, and the corresponding detection limits of the bioagents, can be further significantly improved by the combined use of laser breakdown atomization with resonant laser excitation of metal atoms.

CONCLUDING REMARKS

Clearly, the feasibility of laser spectroscopy as an analytical and diagnostic tool has been sufficiently demonstrated in the past 10 years. The nature of the information that is provided by laser spectroscopy makes these techniques widely applicable, from the quantitative determination of the chemical composition of biological tissue or analyte concentrations in blood or other body fluids to a real-time, *in vivo* rapid diagnostics tools.

In the near future, further advances in laser spectroscopy instrumentation can be expected. CCD detector technology continues to improve and may soon include sensitive and ultrafast detection, reduced read-out noise, increased quantum efficiency, and reduced cost. The advances in laser technology will provide cost-efficient and reliable radiation sources at any desirable wavelength. Therefore, laser spectroscopy is expected in the near future to provide the biomedical community with sensitive new tools for clinical diagnosis and decision-making.

REFERENCES

1. D.V. Martyshkin, R.C. Ahuja, A.Kudriavtsev, and S.B. Mirov, "Effective suppression of fluorescence light in Raman measurements using ultrafast time gated CCD camera," *Rev. Sci. Instrum.*, **75**(3), 630-635 (2004).
2. D.V. Martyshkin, J.G. Parker, V.V. Fedorov, and S.B. Mirov, "Tunable distributed feedback color center laser using stabilized F_2^{+} color centers in LiF crystal," *Appl. Phys. Lett.*, **84**(15) 1-3 (2004).
3. D.V. Martyshkin, S.B. Mirov, Y.X. Zhuang, J.P. Crow, V. Ermilov, J.S. Beckman, "Fluorescence assay for monitoring Zn-deficient superoxide dismutase in vitro" *Spectrochimica Acta A* **59**, 3165-3175 (2003).
4. S.B. Mirov, R.E. Pitt, A. Dergachev, W. Lee, D.V. Martyshkin, O.D. Mirov, J.J. Randolph, L. DeLucas, C.G. Brouillette, T.T. Basiev, Y.V. Orlovskii, O.K. Alimov, I.N. Vorob'ev, "A novel laser breakdown spectrometer for environmental monitoring" in *Air Monitoring and Detection of Chemical and Biological Agents II*, J.Leonelli and M.L.Althouse, Editors, Proceedings of SPIE vol. **3855**, 34-41 (1999).
5. Adar, F., "Evolution and revolution of Raman instrumentation: applications of available technologies to spectroscopy and microscopy." in Handbook of Raman Spectroscopy; edited by, I.R. Lewis and H.G.M. Edwards, (Marcel Dekker, New York, 2001), pp. 11-40.
6. M.D. Morris and D.J. Wallam, *Anal. Chem.* **51** A, 182 (1979).
7. P.R. Carey, in Biochemical Applications of Raman and Resonance Raman Spectroscopies, (Academic Press, New York, 1982).
8. P. P. Yaney, *J. Opt. Soc. Am.* **62**, 1297 (1972).
9. Y.K Voronko, A.B. Kudryavtsev, A.A. Sobol, and E.V. Sorokin, In Spectroscopy of Oxides Crystals for Quantum Electronics (Nauka, Moscow, 1991) pp. 50-100
10. N. Everall, T. Hahn, P. Matousek, A.W. Parker, and M. Towrie, "Picosecond", *Applied Spectrosc.* **55**, 1701 (2001).
11. P. Matousek, M. Towrite, A. Stanley, and A. W. Parker, *Appl. Spectrosc.* **53**, 1485 (1999).

12. T. Tahara, and H. Hamaguchi, *Appl. Spectrosc.* **47**, 391 (1993).
13. A.F. Banishev, Y.K. Voronko, A.B. Kudryavtsev, V.V. Osiko, and A.A. Sobol, *Kristallografia* **27**, 618-620 (1982).
14. T.V. Verdeyen. Laser Electronics, 3rd ed. Prentice Hall Series in Solid State Physical Electronics, edited by N. Holonyak, Jr. (Prentice-Hall, New Jersey, 1995), p. 360.
15. H. Kogelnik and C.V. Shank, *Appl. Phys. Lett.* **43**, 2327 (1972).
16. C.V. Shark, J.E. Bjorkholm, and H. Kogelnik, *Appl. Phys. Lett.* **18**, 395 (1971).
17. V.M. Katarkevich, A.N. Rubinovich, S.A. Ryzhechkin, and T.Sh. Efendiev, *Quantum Electron.* **24**, 871 (1994).
18. W.J. Wadworth, I.T. McKinnie, A.D. Woolhouse, and T.G. Haskell, *Appl. Phys B: Lasers Opt.* **69**, 163 (1999).
19. X.L. Zhu, S.K. Lam, and D. Lo, *Appl. Opt.* **39**, 3104 (2000).
20. K.P. Kretsch, W.J. Blau, V. Dumarcher, L. Rocha, C. Fiorini, J.M. Nunzi, S. Pfeiffer, H. Tillman, and H.H. Hornold, *Appl. Phys. Lett.* **76**, 2149 (2000).
21. C. Ye, K. S. Lam, K. P. Chik, D. Lo, and K. H. Wong, *Appl. Phys. Lett.* **69**, 3800 (1996).
22. K.S. Lam and D. Lo, *Appl Phys. B: Lasers Opt.* **66**, 427 (1998).
23. J.F. Pinto and L. Esterowitz, *Appl. Phys. Lett.* **71**, 205 (1997).
24. T. Kurobori, H. Hinino, Y.Q. Chen, and K. Inabe, *Japanese J. Appl. Phys.* **34**, Pt. 2, 7B, L894-L896 (1995).
25. G.C. Bjorklund, L.F. Mollenauer, and W.J. Tomlinson, *Appl Phys. Lett.* **29**, (1976).
26. T. Kurobori, K. Inabe, and N. Takeuchi, *J. of Phys. D: Appl. Phys.* **16**, L121 (1983).
27. A.Yu. Dergachev and S.B. Mirov, *Optics Communications*, **147**(1-3), 107-111 (1998).
28. T.T. Basiev and S.B. Mirov, Room Temperature Tunable Color Center Lasers (Harwood Academic, Chur, Switzerland, 1994).
29. S. Sasaki, N. Shibata, T. Komori, and M. Iwata, *Neurosci. Lett.* **291**, 44 (2000).

30. T.J. Lyons, H. Liu, J.J. Goto, and A. Nersissian, in Proceedings of the National Academy of Sciences of the United States of America, vol. 93, n. 22, pp.12240 (1996).
31. J.P. Crow, J.B. Sampson, Y. Zhuang, J.A. Thompson, and J.S. Beckman, J. Neurochem. 69, 1936 (1997).
32. J.P. Crow, M.J. Strong, Y. Zhuang, Y. Ye, and J.S. Beckman, J. Neurochem. 69, 1945 (1997).
33. A.G. Estevez, J. P. Crow, J.B. Sampson, C. Reiter, Y. Zhuang, G.J. Richardson, M.M. Tarpey, L. Barbeito, and J.S. Beckman, Science, 286, 2498 (1999).
34. H. Tohgi, T. Abe, K. Yamazaki, T. Murata, E. Ishizaki, and C. Isobe, Ann. Neurol. 46, 129 (1999).
35. S.M. Chou, H.S. Wang, and A. Taniguchi, J. Neurol. Sci. 139, S16-S26 (1996).
36. R.J. Ferrante, L.A. Shinobu, J.B. Schulz, R.T. Matthews, C.E. Thomas, N.W. Kowall, M.E. Gurney, and M.F. Beal, Ann. Neurol. 42, 326 (1997).
37. L. Banci, I. Bertini, D.E. Cabelli, R.A. Hallewell, J.W. Tung, and M.S. Viezzoli, J. Eur. Biochem. 196, 123 (1991).
38. T.D. Rae, P.J. Schmidt, R.A. Pufahl, V.C. Culotta, and T.V. O'Halloran, Science 284, 805 (1999).
39. M. Fleischmann, P.J. Hendra, and A.J. McQuillan, Chem. Phys. Lett. 26, 163 (1974)
40. M. Kerker, O. Siiman, L.A. Bumm, and D.S. Wang, Appl. Opt. 19, 3253-3255 (1980).
41. D.S. Wang and M. Kerker, Phys. Rev. B 69, 4159 (1981).
42. M. Moskovits, Solid State Commun. 32, 59 (1979).
43. M. Moskovits, J. Chem. Phys. 69, 4159 (1978).
44. M. Inoue and K. Ohtaka, J. Phys. Soc. Jpn. 52, 3853 (1983).
45. E.J. Zeman and G.C. Schatz, J. Phys. Chem. 91, 634-53 (1987).
46. F. J. Garcia-Vidal and J. B. Pendry, Phys. Rev. Lett. 77, 1163-1166 (1996).
47. S. Nie and S. R. Emory, Science 275, 1102-1106 (1997).

48. K. Kneipp, H. Kneipp, I. Itzkan, R. R. Dasari, and M. S. Feld, *Chem. Rev.* **99**, 2957-2975 (1999).
49. S. R. Emory, W. E. Haskins, and S. Nie, *J. Am. Chem. Soc.* **120**, 8009-8010 (1998).
50. I. R. Nabiev, H. Morjani, and M. Manfait. *European Biophysics Journal* **19**, 311-316 (1991).
51. E. Koglin and J. M. Séquaris, *Topics in Current Chemistry*. **134**, 3-57 (1986).
52. I.R. Nabiev, K.V. Sokolov, and M. Manfait, in Biomolecular Spectroscopy, edited by R. J. H. Clark and R. E. Hester, (Wiley, New York, 1993). p.287
53. H.Xu, E.J. Bjerneld, M. Kall, and L. Borjesson, *Phys. Rev. Lett.* **83**, 4357-4360, (1999).
54. E.J. Bjerned, P. Johansson, and M. Kall, *Single Mol.* **1**, 239-248 (2000).
55. W. R. Rypniewski, S. Mangani, B. Bruni, P. L. Orioli, M. Casati, and K. S. Wilson, *J. Mol. Biol.* **251**, 282 (1995).
56. I. Ascone, R. Castaner, C. Tarricone, M. Bologanesi, M. E. Stroppolo, and A. Desideri, *Biochem. Biophys. Res. Commun.* **241**, 119 (1997).
57. L. M. Murphy, R. W. Strange, and S. S. Hasnain, *Structure* **5**, 371 (1997).
58. D. Wang, X. Zhao, M. Vargek, and T. Spiro, *J. Am. Chem. Soc.* **122**, 2193-2199 (2000).
59. S. Hashimoto, K. Ono, and H. Takeuchi, *J. Raman Spec.* **29**, 969-975 (1998).
60. Hashimoto, S. Ohsaka, H. Takeuchi, and I. Harada, *J. Am. Chem. Soc.* **111**, 8926 (1989).
61. P. C. Lee and D. Melsel, *J. Phys. Chem.* **86**, 3391-3395 (1982).
62. S. Adrain and J. Watson, "Laser microspectral analysis; a review of principles and applications," *J. Phys. D: Appl. Phys.*, **17**, 1915 (1984).
63. L.J. Radziemski and D.A. Cremers, in Laser-induced Plasmas and Applications, edited by L.J. Radziemski and D.A. Cremers (Marcel Dekker, New York, 1989).
64. L.Moenke-Blankenburg, Laser Microanalysis (Wiley, New York, 1989).

65. V. Majidi and M.R. Joseph, "Spectroscopic applications of laser-induced plasmas," *Critical Review in Anal. Chem.* **23**, 143 (1992).
66. D.A. Rusak, B. Castle, B.W. Smith, and J.D. Winefordner, "Fundamentals and applications of laser-induced breakdown spectroscopy," *Critical Review in Anal. Chem.* **27**, 257 (1997).
67. Y-III. Lee, Y.-J. Yoo, and J. Sneddon, "Recent advances in laser-induced breakdown spectroscopy," *Spectroscopy* **13**, 14-21 (1998).
68. D.A. Cremers, "The analysis of metals at a distance using laser-induced breakdown spectroscopy," *Appl. Spectrosc.* **41**, 572-578 (1987).
69. K.J. Grant, G.L. Paul, and J. O'Neill, "Quantitative elemental analysis of iron ore by laser-induced breakdown spectroscopy," *Appl. Spectrosc.* **45**, 701 (1991).
70. D.K. Ottesen, J.C.F. Wang, and L.J. Radziemski, "Real-time laser spark spectroscopy of particulates in combustion environments," *Appl. Spectrosc.* **43**, 967-976 (1989).
71. D.A. Cremers and J.R. Wachter, "Determination of uranium in solution using laser-induced breakdown spectroscopy," *Appl. Spectrosc.* **41**, 1042-1048 (1987).
72. G. Arca, A. Ciucci, V. Pallachi, S. Rastelli, and E. Tognoni, "Trace element analysis in water by the laser-induced breakdown spectroscopy technique," *Appl. Spectrosc.* **51**, 1102-1105 (1997).
73. S. Nakamura, Y. Ito, K. Sone, H. Hiraga, and K. Kaneko, "Determination of an iron suspension in water by laser-induced breakdown spectroscopy with two sequential laser pulses," *Anal. Chem.* **68**, 2981-2986 (1996).
74. K.Y. Yamamoto, D.A. Cremers, M.J. Ferris, and L.E. Foster, "Detection of metals in the environment using a portable laser-induced breakdown spectroscopy instrument," *Appl. Spectrosc.*, **50**, 222-233 (1996).
75. A. Ciucci, V. Palleschi, S. Rastelli, R. Barbini, F. Colao, R. Fantoni, A. Palucci, S. Ribezzo, and H.J.L. van der Steen, "Trace pollutants analysis in soil by a time-resolved laser-induced breakdown spectroscopy technique," *Appl. Phys. B* **63**, 185-190 (1996).
76. R.M. Measures and H.S. Kwong, "TABLASER: trace (element) analyzer based on laser ablation and selectively excited radiation," *Applied Optics* **18**, 281-286 (1979).

77. W. Sdorra and K. Niemax, "Temporal and spatial distribution of analyte atoms and ions in microplasmas produced by laser ablation of solid samples," *Spectrochimica Acta* **45B**, 917-926 (1990).
78. A. Quentmeier, W. Sdorra, and K. Niemax, "Internal Standardization in Laser induced Fluorescence Spectrometry of Microplasmas Produced by Laser Ablation of Solid Samples," *Spectrochimica Acta* **45B**, 537-546 (1990).

APPENDIX**CALCULATION OF THE DETECTION LIMIT OF MICRORAMAN IMAGING
SYSTEM DILOR XY**

It is assumed that we would use a liquid nitrogen cooled (LNC) CCD camera with the following characteristics: 2000×800 pixels, 30×12 mm active area, 80% quantum efficiency at 740 nm, $S_d=1.4\times 10^{-4}$ (electron/pixel-second) dark current at an operational temperature of 140 K and, read-out noise of $N_r=5$ electrons. The total noise N_t associated with acquisition of spectrum by CCD camera may be expressed as

$$N_t=(N_r^2+N_d^2+N_{ph}^2)^{1/2}, \quad (A1)$$

where N_r is a read-out noise, N_d is a dark-charge noise, and N_{ph} is a photon noise. The photon noise can be neglected due to the low intensity of the acquired signal. We examine the detectability of the system for a one-minute accumulation time with pixel binning in a vertical direction to a supersize pixel (200 pixels). After a one-minute accumulation, the photon shot noise and total noise will be

$$N_d^2=1.4\times 10^{-4}(\text{electrons/pixel-s})\times 60\times 200(\text{pixels})=1.68\text{electrons}, \quad (A2)$$

and

$$N_t=(5^2+1.68)^{1/2}\cong 5.17,$$

since 5.17 counts rms usually means $5.17\times 5=25.9$ counts peak-to-peak noise fluctuations.

The smallest detectable signal will be the signal that is equal to this noise. Since the quantum efficiency of the CCD camera is 80%, the amount of photons corresponding to the noise level will be 32.3. Thus detectability is

$$32.3(\text{photons})/60(\text{s})\times 200(\text{pixels})=2.69\times 10^{-3}(\text{photons/pixel-s}).$$

Let us compare the smallest detectable signal with a fluorescence signal of 10 μM solution of BCDS-SOD1 complexes, which is considered to be an average physiological concentration of SOD1 in cells. We assume that a confocal microscope equipped with a 0.75 numerical aperture objective allows us to collect light from the volume equal to $\sim 10^7$

15 m^3 . That corresponds to 10^{-17} moles or 6.02×10^6 molecules of SOD1, or 12.04×10^6 BCDS-SOD1 complexes. If the power of laser radiation in the focal spot of microscope is equal to 10 mW, the number of excitation photon can be calculated as

$$N_{exc} = \frac{10 \times 10^{-3} W \times 480 \times 10^{-9} m}{6.62 \times 10^{-34} J \cdot s \times 3 \times 10^8 m/s} \approx 2.42 \times 10^{16} \text{ photons/s}, \quad (\text{A3})$$

and photon flux in the focal spot as

$$\Phi = \frac{N_{exc}}{S} = \frac{2.42 \times 10^{16}}{10^{-6} \text{ cm}^2} = 2.42 \times 10^{22} \frac{\text{photons}}{\text{s} \cdot \text{cm}^2}, \quad (\text{A4})$$

where S is an area of the focal spot. The number of photons that BCDS-SOD1 complexes emit under 10 mW excitation at 480 nm is approximately equal to

$$N_{em} = \sigma_{ab} \Phi N \eta, \quad (\text{A5})$$

where σ_{ab} is an absorption cross-section, Φ is a photon flux, and N is a number of BCDS-SOD1 complexes in the studied volume, η is a quantum efficiency of emission from the excited state. The quantum efficiency could be estimated by comparing BCDS-SOD1 complexes fluorescence signal with a signal of the Raman scattering of water. The ratio of the number of fluorescence photons to the number of Raman photons is equal to the ratio of the area (S_{576}) under the Raman band at 576 nm and the area (S_{734}) under the fluorescence band at 734 nm. The S_{734}/S_{576} ration for the 0.15-mM concentration of BCDS-SOD1 complexes corresponds to

$$\frac{S_{734}}{S_{576}} = \frac{\sigma_{ab} \Phi N_0 \eta}{\sigma_R \Phi N_{H_2O}} = \frac{\sigma_{ab} N_0}{\sigma_R N_{H_2O}} \eta = 5.27, \quad (\text{A6})$$

Thus, quantum efficiency of emission from the excited state is equal to

$$\eta = 5.27 \frac{\sigma_R N_{H_2O}}{\sigma_{ab} N_0}, \quad (\text{A7})$$

where $\frac{N_{H_2O}}{N_0} = 3.7 \times 10^5$ is a ratio of number of water molecules to the number of BCDS-SOD1 complexes in 0.15 mM solution. Hence, the number of emitted photons can be obtained by substituting eq.7 in to eq.5.

$$N_{em} = \sigma_{ab} \Phi N \cdot 5.27 \frac{\sigma_R N_{H_2O}}{\sigma_{ab} N_0} = 5.27 \cdot \Phi N \sigma_R \frac{N_{H_2O}}{N_0} = 5.68 \times 10^5 \text{ photons / s}, \quad (A8)$$

The amount of photons collected by the microscope objective can be found as:

$$N_{col} = N_{em} \frac{\Omega_{obj}}{4\pi} T_{obj} = N_{em} T_{obj} \frac{(1 - (1 + NA^2)^{-1/2})}{2} = 3.98 \times 10^4 \text{ photons / s}, \quad (A9)$$

and corresponding light intensity

$$I = N_{col} \cdot h\nu = 1.07 \times 10^{-12} \text{ W / cm}^2, \quad (A10)$$

Where Ω_{obj} is solid angle of collection for microscope objective, T_{obj} is the microscope objective transmission at 740 nm and NA is the microscope objective numerical aperture.

The power transmitted through the spectrometer is given by

$$P = \frac{W \cdot H \cdot A^2}{F^2} \cdot T \cdot I = 4 \cdot W \cdot H \cdot NA_{spec}^2 \cdot T \cdot I = 5.35 \times 10^{-17} \text{ W} \quad (A11)$$

where $H=5$ mm is slit height, $W=200$ μm is slit width, $T=0.5$ is spectrometer transmission at 740 nm, $NA_{spec}=0.05$ spectrometer numerical aperture, and $I=1.07 \times 10^{-12}$ W/cm^2 incident light intensity. The power 5.35×10^{-17} W corresponds to 199 photons per second at 740 nm. Since we illuminate 2000 pixels, the fluorescence signal per pixel-second will be $199(\text{photons/s})/2000(\text{supersize-pixels})=0.1(\text{photon/pixel-s})$ compared to 2.69×10^{-3} (photon/pixel-s) detectibility of the instrument. It corresponds to a signal-to-noise ratio equal to 37 and further demonstrates that BCDS-SOD1 complexes could be detected in single cells.

**GRADUATE SCHOOL
UNIVERSITY OF ALABAMA AT BIRMINGHAM
DISSERTATION APPROVAL FORM
DOCTOR OF PHILOSOPHY**

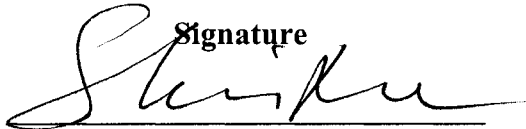
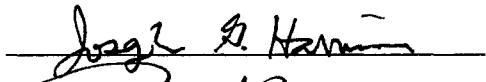
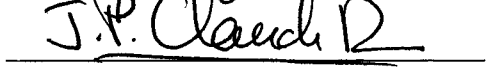
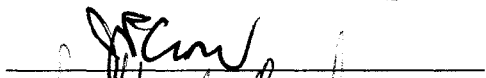
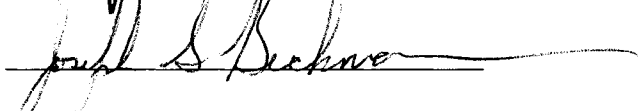
Name of Candidate Dmitri V. Martychkine

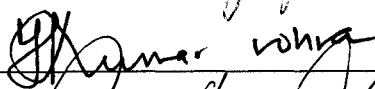
Graduate Program Physics

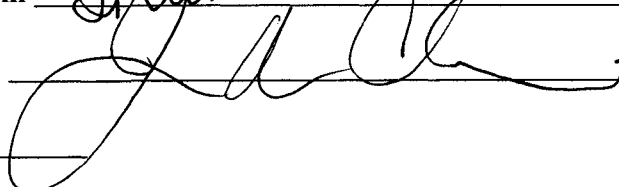
Title of Dissertation Analytical Methods of Laser Spectroscopy for Biomedical
Applications

I certify that I have read this document and examined the student regarding its content. In my opinion, this dissertation conforms to acceptable standards of scholarly presentation and is adequate in scope and quality, and the attainments of this student are such that he may be recommended for the degree of Doctor of Philosophy.

Dissertation Committee:

Name	Signature
<u>Sergey B. Mirov</u> , Chair	
<u>Joseph G. Harrison</u>	
<u>Renato P. Camata</u>	
<u>Juan Pablo Claude</u>	
<u>John Crow</u>	
<u>Joseph S. Beckman</u>	

Director of Graduate Program 

Dean, UAB Graduate School 

Date _____